3D spatial transcriptomics reveals the molecular domain structure of the mouse olfactory bulb

Nell Klimpert*[1], Mihaly Kollo*[2], David H. Brann[3], Chichun Tan[4], David Barry[5], Ying Ma[4], Andreas T. Schaefer[2], and Alexander Fleischmann[1]

Affiliations:

1. Department of Neuroscience and Carney Institute for Brain Science, Brown University, Providence, RI, USA
2. Sensory Circuits and Neurotechnology Laboratory, The Francis Crick Institute, London, UK
3. Department of Neurobiology, Harvard Medical School, Boston, MA, USA
4. Department of Biostatistics and Center for Computational Molecular Biology, Brown University, Providence, RI, USA
5. Crick Advanced Light Microscopy, The Francis Crick Institute, London, UK

* Both authors contributed equally

Corresponding authors: andreas.schaefer@crick.ac.uk, alexander_fleischmann@brown.edu

ABSTRACT

A core organizing principle of the vertebrate brain is its symmetry along multiple axes. However, the structure of these axes, and the precision with which neurons, circuit modules, and brain regions align to them, remain poorly understood. Here, we used 3D spatial transcriptomics to reconstruct the anatomical and molecular organization of the mouse olfactory bulb. We mapped the positions of nearly one thousand molecularly distinct glomeruli, the structural and functional units of odor processing, revealing highly symmetric organization across brain hemispheres. Within each bulb, we defined a curved axis of symmetry that divides pairs of sister glomeruli. Gene expression programs in olfactory sensory neurons predicted glomerular position with near-glomerular resolution. However, glomerular symmetry was disrupted in deeper layer mitral and granule cells, suggesting a reorganization of olfactory bulb output pathways. Our findings provide the first comprehensive map of the molecular domain structure of the olfactory bulb.

INTRODUCTION

Brains are highly variable in size, structure, and complexity across the animal kingdom, yet a fundamental shared feature across all vertebrate brains is bilateral symmetry: brain regions are duplicated along the midline, resulting in mirror-symmetric left and right hemispheres. Furthermore, even within hemispheres, brain areas often exhibit mirror-symmetric maps, for example in auditory and visual cortex[1,2]. Despite such overall symmetry, many structural and functional asymmetries have been described. Cortical areas involved in auditory processing and vocalization in humans and non-human primates are larger in the left hemisphere[3–5]. In birds including pigeons and chickens, visual pathways are dominant in the left hemisphere[6,7], and in the zebrafish brain, visual and olfactory information processing is lateralized in structurally asymmetric habenulae[8,9]. At what resolution, then, are brains symmetric? Limitations in the spatial resolution of fMRI make it difficult to identify differences in the human brain beyond regional asymmetries. In the smaller brains of invertebrates, resolving hemispheric symmetry at the cellular level is possible; however, cellular resolution for mammalian brains with millions of neurons is currently beyond reach. The olfactory system provides a unique opportunity to probe symmetry at the resolution of independent structural and functional units: glomeruli in the mouse olfactory bulb (OB) represent segregated channels of information processing that are approximately 100 μm in diameter.

Glomerular activity represents the activation of olfactory sensory neurons (OSN) in the olfactory epithelium (OE). Glomeruli, in turn, activate mitral and tufted cells, which form microcircuits with deep-layer inhibitory granule cells to route information to the olfactory cortex. OSNs expressing one of approximately 1,100 odorant receptor (OR) genes[10,11] converge their axons to ~2 glomeruli per OB hemisphere[12–18]. Prior work has described mirror-symmetry across OB hemispheres, which may be functionally relevant for stereo-sampling odor information via inter-hemispheric connections through the anterior olfactory nucleus[13,19,20]. In addition, mirror-symmetry exists within each OB hemisphere[21,22], with each OSN type believed to innervate one medial and one lateral glomerulus. However, whether this overall symmetry reflects a broad compartmentalization of the OB or the precise, mirrored arrangement of individual glomeruli remains unknown. Moreover, it is not known whether these duplicated glomerular inputs map onto molecularly distinct output domains.

Here, we generated a comprehensive, three-dimensional molecular map of the mouse OB. We performed sequencing-based spatial transcriptomics on 200 consecutive tissue sections of OB and captured OR transcripts within glomeruli to confidently define the positions of 968 glomeruli. We compare the mirror-symmetric organization of glomerular maps across hemispheres, and we identify lateral and medial domains separating sister glomeruli within each OB. Using single-cell gene expression data from OSNs, we uncover genetic signatures

that can predict glomerular position with near-glomerular accuracy. Finally, we show that the symmetry of the glomerular input layer is restructured in the mitral and granule cell output layers.

RESULTS

3D spatial transcriptomics of the mouse olfactory bulb

To generate a comprehensive molecular map of the mouse OB, we used sequencing-based spatial transcriptomics (Visium V1, 10x Genomics) to capture mRNA transcripts from serial sections of the OB (200 cryosections, 10 µm thick; See Methods, **Fig. 1a**, **Fig. S1**). The technology utilizes printed microarrays with 55µm diameter mRNA capture spots to integrate gene expression and spatial information for individual tissue sections. We initially assessed the quality of our RNA sequencing data by integrating data across all sections. Our dataset contained 190,445 capture spots with, on average, 4,547 unique genes and 13,941 unique transcripts per capture spot (**Fig. 1b**). Next, we Leiden-clustered the capture spots based on their transcriptomic similarity and deconvolved these clusters with an established snRNA-seq reference dataset of mouse OB to evaluate their cellular composition (Methods, **Fig. 1c-e**, **Fig. S2a and b**). We found that capture spots clustered in a layer- and cell-type-specific manner (**Fig. 1d-f**). For example, spots in the mitral cell layer captured high levels of the known mitral and tufted cell marker *Cdhr1*[23–25], spots in the glomerular layer contained high levels of the external tufted cell marker *Ly6g6e*[25], and spots in the outer olfactory nerve layer contained the known OSN marker *Omp*[26,27] (**Fig. 1f**).

To comprehensively determine glomerular identity, we next tested whether spatial transcriptomics could capture OR mRNA transcripts in OSN axons in the OB. In single tissue sections, individual OR genes were typically expressed in focal regions in the glomerular layer. For example, *Olfr124*, *Olfr1420*, *Olfr209*, and *Olfr676* were each expressed in 2-8 capture spots centered over individual glomeruli, with minimal background expression (**Fig. 1g**, **Fig. S3a**). OR transcript capture was validated using immunohistochemistry on a small set of saved tissue sections, where expression of *Olfr6* and *Olfr1507* were localized within M50 and MOR28 glomeruli, respectively, in neighboring sections (**Fig S3b**). Furthermore, expression of a single OR gene was consistently detected around the same glomerulus in consecutive sections. For example, expression of *Olfr3* was restricted to 4-7 capture spots surrounding a single visually identifiable medial glomerulus across 8 consecutive sections (**Fig. 2a**).

To integrate gene expression and spatial information in 3D, we combined manual annotation of over 2,500 glomeruli based on the distribution of nuclei in the reference histology images with computer vision to align tissue sections (**Fig. 2b, Fig S4**) (see Methods). We then transformed the capture spot coordinates and corresponding gene expression data to align

with this morphological reconstruction. We found that sites of high OR expression aligned with morphologically identified glomeruli in 3D. For example, expression of *Olfr3* was localized to 4 restricted sites across both bulbs, consistent with one lateral and one medial glomerulus per bulb (**Fig. 2c**). Moreover, low levels of OR expression often extended from focal regions of high expression in glomeruli to the outer nerve layer, consistent with localization to OSN axons (**Fig. 2c and d**). Overall, our dataset contains OR gene expression data from 997 out of 1,135 annotated OR genes. OR genes varied widely in abundance, likely due to variable expression and capture efficiency[28,29]. We categorized these expression patterns based on the strength of OR expression and parameters describing spatial distribution (**Fig. 2e-h**). Out of the 997 OR genes captured in the dataset, 784 showed expression with a structured and spatially clustered distribution of spot counts with variable expression levels ("Low", "Medium", and "High"). The remaining 61 OR genes showed low levels of background expression throughout the tissue volume ("Diffuse"). Taken together, we have generated the first 3D spatial transcriptomics data set with comprehensive gene expression information, including OR expression localized to individual glomeruli, across the entire mouse OB.

A computational model to quantify glomerular identity and position

We next used a Bayesian framework to quantify glomerular position. We modeled the distribution of OR gene expression at capture spots surrounding a glomerulus based on glomerular geometry, assuming that the detected expression is linearly dependent on the total overlap between the glomerular volume and the detected spots (see Methods, **Fig. S5a**). We generated predicted count values in each capture spot for any given set of putative glomeruli, defined by their position, radius, and expression level. We then optimized the model by iteratively updating the distributions of these glomerular parameters, comparing them to observed OR gene expression using a Markov Chain Monte Carlo (MCMC) algorithm (see Methods, **Fig. S5b and c**). The resulting Probabilistic Glomerulus Position (PGP) model generated putative locations with different levels of probabilities for 906 ORs. We then confirmed glomerular identity for glomeruli that were assigned a high probability by the model using human expert inspection of predicted positions and raw gene expression data (**Fig. S6a and b**). After expert curation, the PGP model yielded a glomerular map containing the quantified positions of glomeruli expressing 233 OR genes, yielding a map of 673 glomeruli (**Fig. 3a**).

Visual inspection of these glomeruli revealed two axes of symmetry: glomeruli expressing the same OR were bilaterally mirror symmetric between hemispheres and within each OB. We compared the glomerular maps between the bulbs to quantify symmetry. We first aligned the geometric positions of the two hemispheres to counteract relative rotation and distortions during tissue processing. We then measured the distance between corresponding glomeruli

of the same molecular identity from the two OB. Our analysis revealed a remarkably high upper bound of inter-bulbar symmetry, with a mean deviation of 231 μm from perfect symmetry (**Fig. 3b and c**).

Next, we assessed the symmetry of the glomerular map within each OB hemisphere. Considering the complex, curved three-dimensional geometry of the OB glomerular layer, we used a dual autoencoder (AE) model to describe the relative spatial arrangement of sister glomeruli expressing the same OR. This algorithm uses a two-layer encoder network to map the positions of glomeruli based on the PGP model into a two-dimensional embedding, then reconstructs glomerular positions across bulbs and sister glomerulus positions within each bulb using two identical decoder networks (see Methods, **Fig. 3d**, **Fig. S7 a-f**). The resulting encoding revealed that sister glomeruli were well separated by vector direction in the latent space (**Fig. 3e**, **Fig. S8a and b**), corresponding to medial and lateral glomeruli. This allowed us to define an intra-hemispheric axis of symmetry and assign a medial and lateral label to each glomerulus based on its relative position to its sisters in an unsupervised manner (**Fig. 3e, Fig S8c and d**). Finally, we utilized the predicted positions of sister glomeruli proposed by the autoencoder trained on curated glomeruli to confirm the validity of the entire set of putative glomeruli generated by the PGP model (**Fig. 3a**, see Methods). The resulting glomerular map is comprised of 968 high-confidence glomeruli expressing 255 OR genes (**Fig. 3g**, **Fig. S9**).

We next analyzed the relative positions of sister glomeruli. This analysis revealed that sister glomeruli expressing the same OR are clearly separable along a medial-to-lateral axis within each hemisphere (**Fig. 3f**). To characterize the organization of individual glomeruli along this axis, we ranked the positions of glomeruli within the medial domain (see Methods). Glomerular ranks were well-preserved when compared along the lateral domain. Support vector machines trained on lateral glomerular positions could accurately predict the medial glomerular ranks of lateral glomeruli (**Fig. 3h and i**). Furthermore, the pairwise distances of glomerular positions in each domain were well correlated with each other, both locally and across the entire OB (**Fig. 3j**). Together, our data provide a detailed, quantitative description of glomerular identity and position, revealing a glomerular map that is mirror-symmetric between hemispheres and duplicated with a remarkably high fidelity within each OB.

The molecular organization of the glomerular map

Prior work has implicated ORs type, sequence similarity, and non-OR gene expression in the OE in determining the organization of the glomerular map[13,15,30–32]. However, how these factors contribute to positioning the entire glomerular map is unknown. Therefore, we next sought to determine the extent to which OR identity and OSN gene expression predict glomerular position. Canonical ORs can be divided into two classes, with approximately 130

class I and 950 class II ORs[33,34]. Consistent with prior work[35,36], glomeruli expressing class I ORs were found in the dorsal-most part of the OB, while glomeruli expressing class II ORs were found throughout the rest of the OB (**Fig. 4a**). For class II ORs, we observed a moderate but significant correlation between their phylogenetic similarity and glomerular positions, with more similar pairs of ORs located closer in space (**Fig. 4b and c**). Furthermore, we found that the pairwise glomerular distance distributions were smaller on average for OR pairs within the same chromosomal cluster (**Fig. S10a-c**). Finally, chromosomal clusters with ORs that were phylogenetically more similar had, on average, closer pairs of glomeruli (**Fig. 4c**). For example, a population of glomeruli expressing a cluster of phylogenetically similar ORs located on chromosome 10 was restricted to the anterior portion of the OB; this cluster corresponds to the recently identified subtype of OSNs that express the transmembrane protein CD36[37] (**Fig. S10d**). These results suggest a significant correlation between OR sequence similarity and genomic proximity with glomerular position for glomeruli/receptors within the class II domain.

We next examined the relationship between the molecular organization of the glomerular map and gene expression programs in the OE. Recent work using single-cell RNA-sequencing (scRNA-seq) revealed that OSNs in the OE expressing a given OR have a unique transcriptional identity[17,38,39]. Therefore, we asked whether such variation in the expression of non-OR genes could predict glomerular positions. We first selected 180 well-characterized axon guidance and cell adhesion molecules and assessed how well the expression of these genes, measured via scRNA-seq of OSNs, could predict the location of glomeruli, measured via spatial transcriptomics. We observed that the expression of these axon guidance genes strongly correlated with glomerular positions. Furthermore, individual genes had similar correlations with positions from the lateral and medial glomeruli, suggesting that such genes may influence the observed symmetry in the glomerular maps across the medial and lateral hemispheres (**Fig. S10g**). Elastic-net-regularized linear regression models trained on these axon guidance genes accurately predicted glomerular positions for each of the anterior-posterior and dorsal-ventral axes, with an average regression prediction error of 170.9 μm for lateral glomeruli and 160.3 μm for medial glomeruli along the A-P axis, and 183.3 μm for lateral glomeruli and 189.2 μm for medial glomeruli along the D-V axis (**Fig. 4f, Fig. S10e and f**). Hierarchical clustering of the expression patterns of these genes revealed sets of genes with distinct patterns of correlations with glomerular positions, two of which mapped onto the anterior-posterior and dorsal-ventral axes (**Fig. 4d**). These clusters contained axon guidance genes that have previously been shown to regulate glomerular positions, such as *Robo2*, *Sema3f*, *Nrp2*, and *Slit1*[40–42](**Fig 4d**), as well as genes whose functions in glomerular map formation remain uncharacterized (**Fig S11a**).

Finally, we asked whether the transcriptional variation across OSNs is reflected in the glomerular map. We recently characterized ~1,300 “highly-variable genes” (HVGs) that could accurately distinguish between OSNs expressing different ORs[39]. We therefore tested the extent to which the expression of these HVGs could predict glomerular positions. We observed that HVG expression correlated with glomerular positions and that elastic net models trained on their expression across OSN subtypes could accurately predict the glomerular positions of their respective ORs, with an average regression prediction error of 110.5 μm for lateral glomeruli and 118.8 μm for medial glomeruli along the A-P axis, and 146.7 μm for lateral glomeruli and 157.4 μm for medial glomeruli along the D-V axis (**Fig. 4f and g, Fig. S10e**). Examination of HVGs predictive of glomerular position identified both known and novel genes. For example, the family of NFI transcript factors predicted the positions of ventral glomeruli, whereas the expression of genes like *Acsm4* and *Cartpt* was enriched in OSN subtypes that project to the dorsal part of the OB[43,44](**Fig. 4e**). Additionally, genes downstream of OR signaling like phosphodiesterase enzymes and *Pkia* were also predictive of glomerular positions; this observation was especially robust along the anterior-posterior axis, consistent with prior work demonstrating how glomerular positions along this axis are influenced by ligand-independent OR activity[45] (**Fig S11b**). Finally, we observed that the expression of synaptic genes like *Syt1* varied as a function of projection patterns along the dorsal-ventral axis, suggesting ways in which OSN function might vary across the OB (**Fig. 4e**).

In summary, by integrating transcriptomics datasets from the OE and OB, we reveal that transcriptional differences across OSN subtypes reflect their connectivity with distinct glomerular domains, are predictive of the stereotyped glomerular positions along each OB axis, and may correspond to differences in OSN function and signaling along these axes.

Mitral cell projection neurons and deep-layer granule cells exhibit molecular structure along alternative axes

Finally, we asked whether the duplicated glomerular input maps onto distinct molecular domains in the mitral cell output layer and deep-layer granule cells. To restrict our analysis to defined cell types and layers, we isolated capture spots from the Leiden Clusters (**Fig 1c and d**). From these clusters, we selected those representing deep granule cells (Leiden Cluster 1), superficial granule cells (Leiden Clusters 8 and 9), and mitral cells (Leiden Cluster 6) based on their alignment with morphology (**Fig 4h and i**). We then determined, for each layer, the axis angle for each gene that maximizes differential gene expression across the axis (see Methods, **Fig 4j**). Significantly differentially expressed genes and gene signatures exhibited a range of structured expression patterns along multiple different axes (**Fig 4j and k**). However, we did not observe any preferential alignment of these gene expression patterns with the glomerular axis of symmetry (Red line, **Fig 4j**). These data suggest that the symmetry defined

by OR identity in the glomerular layer is reorganized, rather than mirrored, in the mitral and granule cell layers.

DISCUSSION

We here provide a detailed 3D map of the molecular structure of the mouse OB and determine the precise positions of hundreds of glomeruli. The spatial arrangement of molecularly distinct glomeruli defined two axes of symmetry. The first was the midline, dividing mirror-symmetric glomerular maps in the left and right OB, while the second was within each OB, at the boundary between the medial and lateral duplications of the map. The organization of mitral and granule cells did not mirror this glomerular layer symmetry. By integrating spatial transcriptomics and single-cell RNA sequencing data, we found that gene expression programs in the OE could determine glomerular positions with near-glomerular resolution.

Symmetry of the glomerular map

In the OB, glomeruli and their connected microcircuits are functional units that route odor information from primary sensory neurons in the OE to the olfactory cortex. An intriguing feature of the glomerular map is its apparent mirror symmetry across hemispheres and within each OB. Based on positional information from hundreds of glomeruli and a dual autoencoder model to account for the complex geometry of the glomerular layer, we identify a curved plane as the axis of this intra-hemispheric symmetry, based on the relative positions of sister glomeruli expressing the same OR along the curved plane. This analysis revealed that the locations of sister glomeruli were aligned with precision along a medial-to-lateral axis of symmetry, such that the ranks of lateral glomeruli can be accurately predicted from the ranks of medial glomeruli.

Prior work suggests that mirror symmetry in the glomerular map may be critical for olfactory navigation[46–50]. Animals utilize olfactory stereo sampling to sample dynamic odor plumes, and OSNs from the medial (septum) and lateral (turbinate) olfactory epithelium project to the medial and lateral OB[13]. Thus, differences in odorant-receptor interactions across the olfactory epithelium may result in the differential activation of the lateral and medial glomerular domains of the OB. The axis of intra-hemispheric symmetry we define will allow for future research to elucidate the functional relevance of mirror-symmetric glomerular maps. More generally, the glomerular map provides a unique experimental model for determining the molecular mechanisms that establish or disrupt symmetry in the brain, for example by manipulating the expression of symmetry-breaking genes[51–53].

What is the relationship between the glomerular map and the organization of neurons in the deeper layers of the OB? Each glomerular column contains a set of mitral and tufted cell

projection neurons that route information to downstream cortical areas, and molecularly distinct mitral and tufted cell subtypes preferentially project to different downstream cortical regions[25,54,55]. Moreover, mitral and tufted cell activity is modulated by local inhibitory neurons, including periglomerular cells and deep-layer granule cells[56–58]. While our analysis reveals spatial structure of gene expression in the mitral and granule cell layers, our results suggest that the axis of glomerular symmetry is reorganized, rather than mirrored, in the molecular patterns of output neurons. This reorganization may provide a mechanism to decorrelate the duplicated glomerular input channels.

The molecular structure of the glomerular map

A range of diverse molecular mechanisms has been proposed to control glomerular positioning, including OR identity, intrinsic signaling, and graded expression of axon guidance genes during development[59–61]. However, prior studies aiming to disrupt the position of glomeruli through perturbations in the expression of individual ORs or axon guidance genes resulted in only partial alterations of the glomerular map. Thus, precise glomerular positioning likely relies on multiple complementary mechanisms for axon guidance.

By utilizing sequencing-based spatial transcriptomics, we gain access to the entire OB transcriptome, allowing us to comprehensively assess gene expression programs along axes of glomerular symmetry. We identified a modest but significant correlation between glomerular position and phylogenetic OR similarly, consistent with a model that comprehensive gene expression programs beyond OR identity determine glomerular position[17,18,62]. We next assessed whether the unique transcriptomic identity of OSNs contributes to glomerular positioning. We found that the expression of a set of characterized axon guidance genes and cell adhesion molecules predicted the position of glomeruli with an accuracy of ~200 μm. This prediction accuracy was further improved to 110-150 μm, near glomerular accuracy, when including a set of highly variable genes (HVGs) expressed in OSNs in the OE[39]. Together, these results suggest that gene expression programs in the OE, which provides sensory input to the OB, are strongly correlated with the molecular organization of the glomerular map.

In summary, the ability to map the organization of glomeruli, the structural and functional units of information processing in the olfactory bulb, has revealed the striking precision with which molecular information determines the spatial organization of highly symmetric glomerular maps. By integrating this structural information with functional approaches, future experiments will allow us to unravel the molecular-anatomical basis for information processing in the olfactory system.

AUTHOR CONTRIBUTIONS

Conceptualization: NK, MK, ATS, AF; methodology: NK, MK, DHB, DB, CT, YM; investigation: NK, MK, DHB, DB, CT; visualization: NK, MK, DHB, CT; funding acquisition: NK, YM, ATS, AF; project administration: AF, ATS; supervision: NK, MK, YM, ATS, AF; writing - original draft: NK, MK, DHB, ATS, AF; writing - review & editing: NK, MK, DHB, CT, DB, YM, ATS, AF

COMPETING INTERESTS

Authors declare that they have no competing interests.

ACKNOWLEDGEMENTS

We thank Joakim Lundeberg, Kim Thrane, and Annelie Mollbrink from the Department of Gene Technology, KTH Royal Institute of Technology in Stockholm, Sweden for support in optimizing the spatial transcriptomics protocol to capture OR transcripts in OB. We thank Lindsay Scarpitta and Pieter Faber from the Genomics Facility at the University of Chicago for sequencing services, and Christoph Schorl from the Genomics Facility at Brown University for quality control of cDNA libraries. We thank Nicole Eckart from 10x Genomics for excellent technical support, Sina Tootoonian for advice on modeling, and Carles Bosch from the Crick Institute, as well as Norman Rzepka and Florian Meinel from Scalable Minds for their help with tissue alignment. We thank David Berson, Tom Bozza, Kevin Franks, and Anthony Crown for critical comments on the manuscript, and we thank Gilad Barnea for providing antibodies and for critical comments on the manuscript.

FUNDING

NK is supported by the National Science Foundation Graduate Research Fellowship Program under Grant No. 2040433. CT is supported by an American Cancer Society - Institutional Research Grants pilot award IRG-23-1154606-01-IRG. Work in the AF lab was supported by an NIH U19NS112953-01 award and the Robert J and Nancy D Carney Institute for Brain Science. Carney Institute computational resources used in this work were supported by the NIH Office of the Director grant S10OD025181. Work is the ATS lab was supported by a Physics of Life grant (EP/W024292/1) and the National Science Foundation/Canadian Institute of Health Research/German Research Foundation/Fonds de Recherche du Québec/UK Research and Innovation–Medical Research Council Next Generation Networks for Neuroscience Program (Award No. 2014217). This work was supported by the Francis Crick Institute, which receives its core funding from Cancer Research UK (FC001153 to A.T.S.), the UK Medical Research Council (FC001153 to A.T.S.), and the Wellcome Trust (FC001153 to A.T.S.). For the purpose of Open Access, the author has applied a CC BY public copyright license to any Author Accepted Manuscript version arising from this submission.

Figure 1

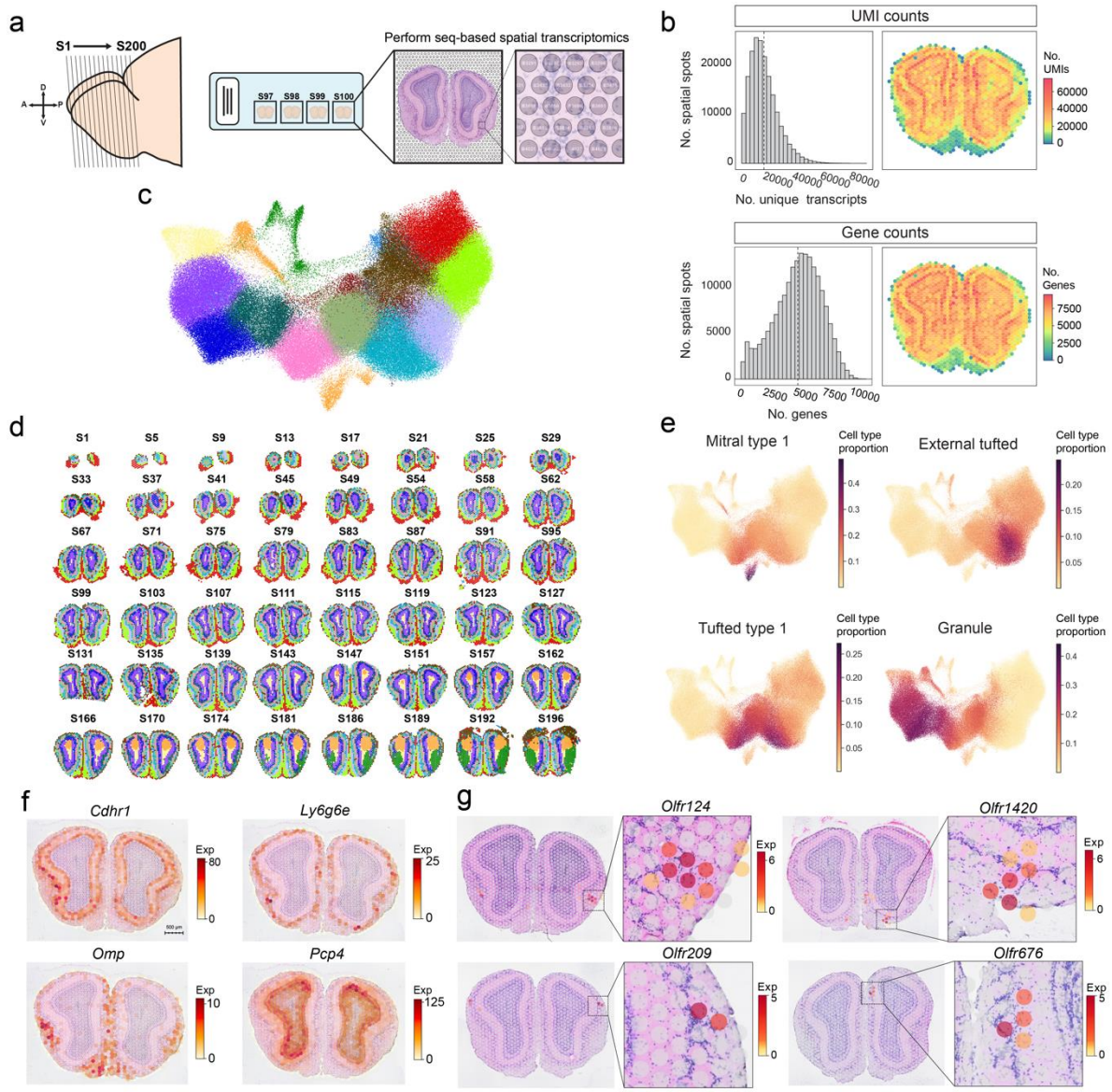
a
S1
S200
D
A
P
V
S97
S98
S99
S100
Perform seq-based spatial transcriptomics
b
UMI counts
No. spatial spots
No. unique transcripts
No. UMIs
Gene counts
No. genes
No. Genes
c
d
e
Mitral type 1
External tufted
Tufted type 1
Granule
Cell type proportion
f
Cdhr1
Ly6g6e
Omp
Pcp4
Exp
g
Olfr124
Olfr1420
Olfr209
Olfr676

Figure 1: Generation of comprehensive molecular map of mouse olfactory bulb using sequencing-based spatial transcriptomics

(a) Schematic of spatial transcriptomics experiment. 200 consecutive sections of OB tissue were mounted onto capture probe microarrays. Sections were stained with hematoxylin and eosin and imaged, then tissue was permeabilized to allow mRNA capture. 200 individual libraries were prepared, providing spatially localized gene expression data.

(b) RNA quality control. **Top:** Histogram of the average numbers of unique transcripts, or unique molecular identifiers (UMIs) per capture spots. On average, 13,941 UMIs were captured per capture spot across all 200 tissue sections; heatmap shows a representative image of transcript numbers in a single section. **Bottom:** Average numbers of genes per capture spot. On average, 4,547 genes were captured per capture spot across 200 sections; heatmap shows a representative image of the number of genes in a single section.

(c) Leiden clustering of 190,445 integrated capture spots across 200 tissue sections.

(d) Capture spots colored by Leiden cluster in 48 representative tissue sections in the dataset, revealing clustering based on OB layers.

(e) Identification of capture spot cell type identities by deconvolution of spatial transcriptomics data with reference OB scRNA-seq. Color represents cell type proportion in capture spots.

(f) Raw expression of known genetic markers for mitral and tufted cells (*Cdhr1*), external tufted cells (*Ly6g6e*), olfactory sensory neurons (*Omp*), and granule cells (*Pcp4*).

(g) Examples of normalized gene expression of Olfr124, Olfr676, Olfr1420, and Olfr209 in single tissue sections. High normalized OR expression is restricted to 3-8 capture spots surrounding a single glomerulus.

Figure 2:

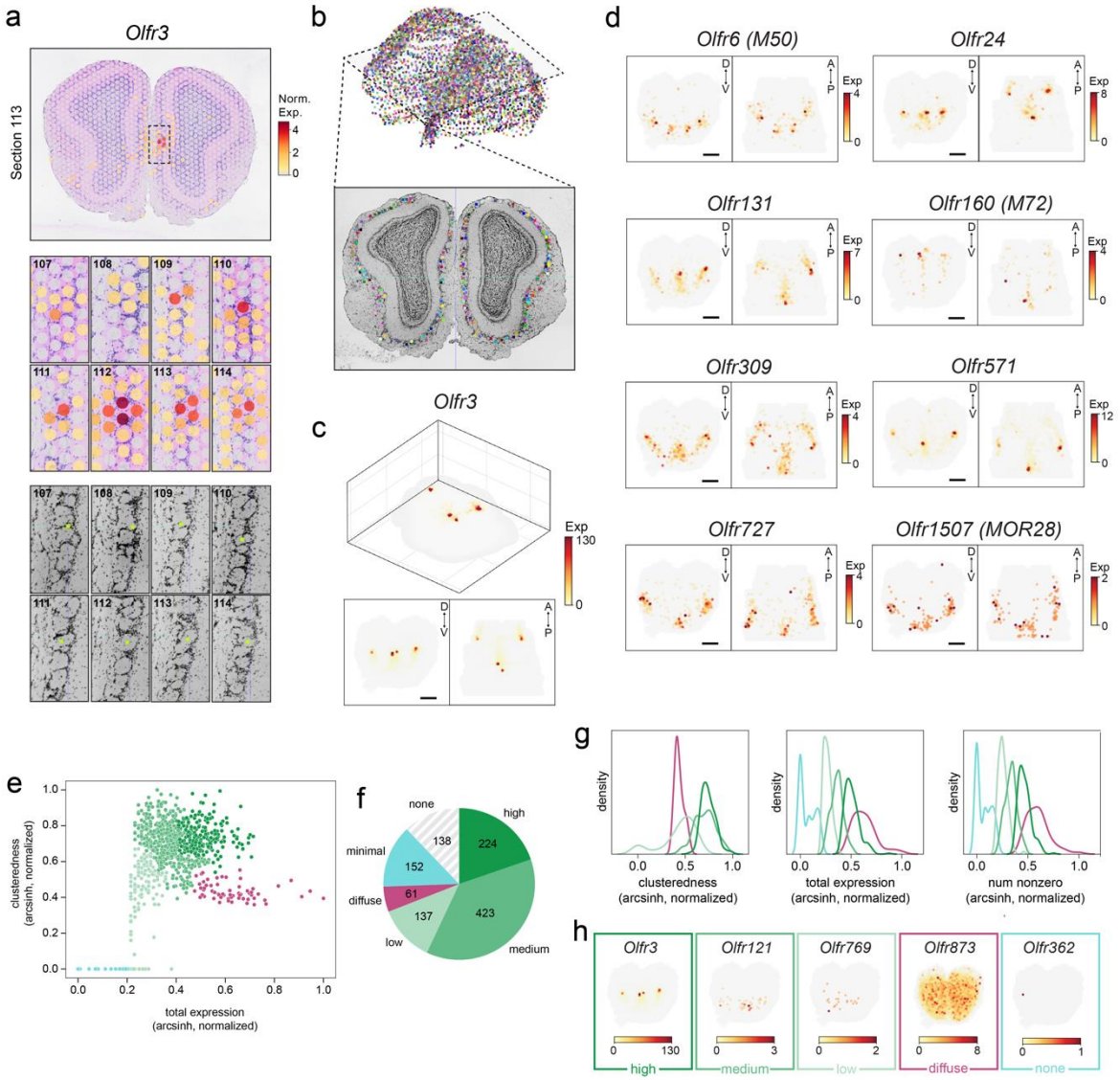
a
Olfr3
Section 113
Norm. Exp.
4
2
0
107
108
109
110
111
112
113
114
b
c
Olfr3
Exp
130
0
D
V
A
P
d
Olfr6 (M50)
Olfr24
Olfr131
Olfr160 (M72)
Olfr309
Olfr571
Olfr727
Olfr1507 (MOR28)
e
clusteredness (arcsinh, normalized)
total expression (arcsinh, normalized)
f
none
high
minimal
diffuse
low
medium
138
224
152
61
137
423
g
density
clusteredness (arcsinh, normalized)
total expression (arcsinh, normalized)
num nonzero (arcsinh, normalized)
h
Olfr3
Olfr121
Olfr769
Olfr873
Olfr362
high
medium
low
diffuse
none

Figure 2: Morphological alignment and transformation of capture spots in 3D

(a) Top: Log2 normalized expression of *Olfr3* is overlayed against H&E image. High normalized expression is observed in capture spots surrounding a single glomerulus across consecutive sections. **Bottom:** The center of a single glomerulus is annotated across 8 consecutive sections. Glomerular annotations were used to refine the alignment of the glomerular layer.

(b) 3D visualization of the 2550 manually annotated, histologically defined glomeruli, with each colored cube representing the center of a single glomerulus. Bottom shows the coronal view of a single section.

(c) Raw expression of Olfr3 visualized in 3D (top) and as a maximum Z-projection along to anterior-to-posterior axis and Y-projection along the dorsal-to-ventral axis (bottom). 3D representation of OR expression reveals defined areas of high expression consistent with glomeruli.

(d) Raw expression of 9 OR genes, visualized as a maximum Z-projection (left) and Y-projection (right). Examples show areas of high expression (red) vs. low expression (yellow) and illustrate variability in expression across OR genes.

(e) Classification of gene expression patterns based on clusteredness of capture spots expressing the OR and total expression across the tissue. Clusteredness is determined as the silhouette score of clusters after a 3D k-means clustering (4 clusters) of spots.

(f) Expression patterns across the 1135 olfactory genes were examined. Expression was detected in 82% of genes with variable expression levels and clusteredness, 5% showed diffuse, non-clustered expression, and 12% were not detected.

(g) Distribution of descriptors (clusteredness, total expression, number of nonzero capture spots) across different expression categories.

(h) Example raw data showing the Z-projection of a single example OR gene from each cluster.

Figure 3:

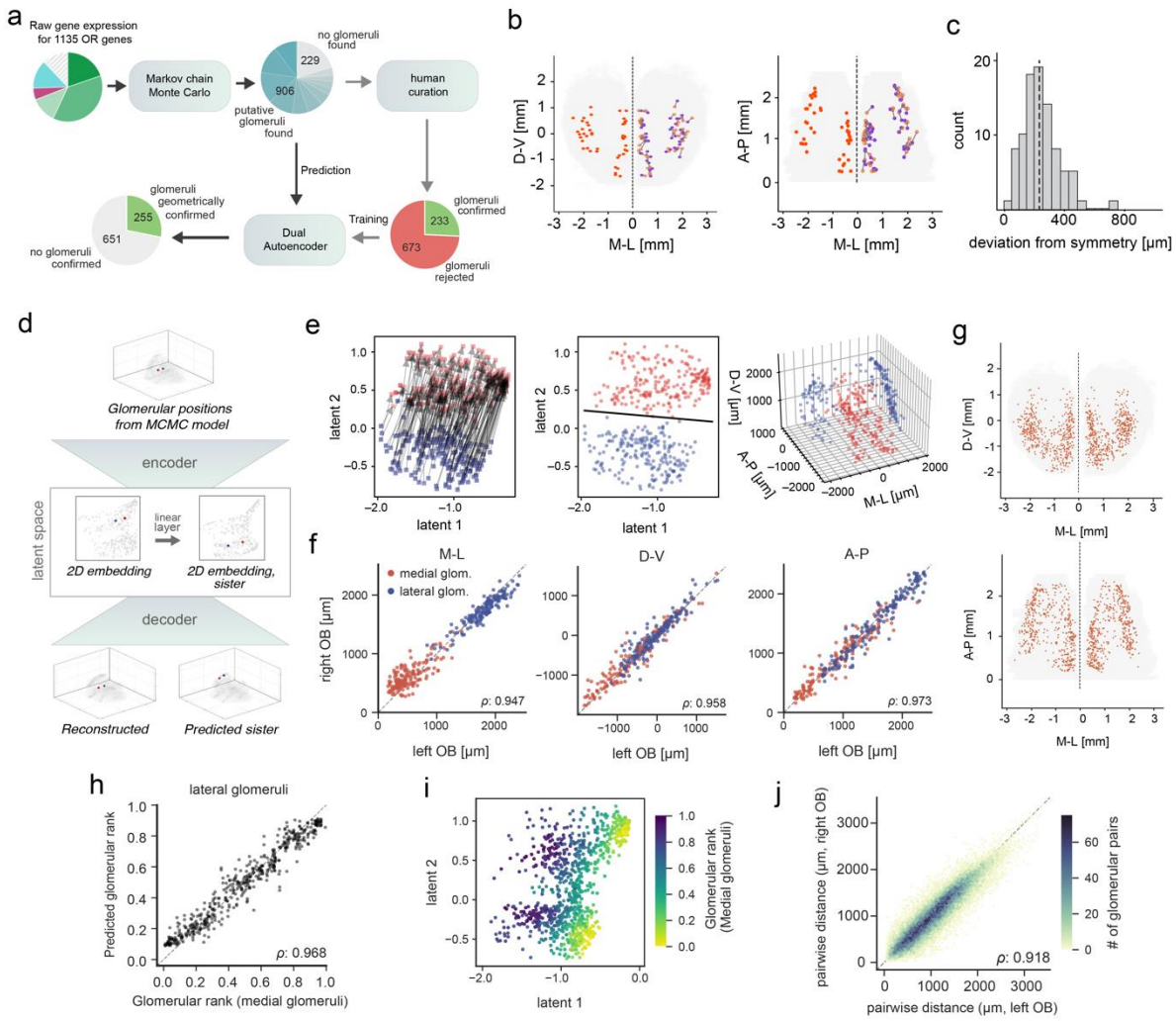
a
Raw gene expression for 1135 OR genes
Markov chain Monte Carlo
no glomeruli found
229
906
putative glomeruli found
human curation
Prediction
glomeruli geometrically confirmed
255
651
no glomeruli confirmed
Dual Autoencoder
Training
glomeruli confirmed
233
673
glomeruli rejected
b
D-V [mm]
M-L [mm]
A-P [mm]
c
count
deviation from symmetry [µm]
d
Glomerular positions from MCMC model
encoder
latent space
linear layer
2D embedding
2D embedding, sister
decoder
Reconstructed
Predicted sister
e
latent 2
latent 1
D-V [µm]
A-P [µm]
M-L [µm]
f
M-L
D-V
A-P
medial glom.
lateral glom.
right OB [µm]
left OB [µm]
ρ: 0.947
ρ: 0.958
ρ: 0.973
g
D-V [mm]
M-L [mm]
A-P [mm]
h
lateral glomeruli
Predicted glomerular rank
Glomerular rank (medial glomeruli)
ρ: 0.968
i
latent 2
latent 1
Glomerular rank (Medial glomeruli)
j
pairwise distance (µm, right OB)
pairwise distance (µm, left OB)
ρ: 0.918
# of glomerular pairs

Figure 3: The quantified positions of 968 glomeruli reveal the defined mirror symmetry of the glomerular map

(a) Schematic of the process used to position glomeruli from OR gene expression. Initial identification of putative glomeruli was done using a probabilistic spatial gene expression PGP model of count values in proximity to glomeruli. OR genes were categorized based on differences in expression patterns (see also Fig. 2 f-i). The PGP model fitted putative glomeruli at various confidence levels (the hue of the blue segments represents p=<0.1 to =1 for the glomeruli of 906 ORs). A curated dataset of confirmed glomeruli was then defined by human experts (see Methods), which was used to train a dual autoencoder (AE) model to predict the location of sister glomeruli of each putative glomerulus in the unsupervised output of the PGP model.

(b) Left and right bulbs were aligned based on the positions of 233 glomeruli identified by the PGP model and confirmed by expert curation. The resulting left and right glomerular maps show high symmetry, with a close spatial alignment corresponding left-side and right-side glomeruli.

(c) The resulting left and right glomerular maps show high symmetry, with a mean deviation of 231 µm between corresponding glomeruli.

(d) An autoencoder (AE) model predicts the location of sister glomeruli for each putative glomerulus identified by the PGP model. 3D glomerular positions are projected onto a 2D embedding space. A single linear layer is used to predict the 2D latent embedding of sister glomeruli from the original glomeruli. The same decoder is used to decode the positions into final 3D sister glomerulus positions.

(e) Left: Curated medial (red) glomeruli share the same vector directions in the latent representation and are spatially separated from lateral (blue) glomeruli. Middle: Linear separation of the medial (red) and lateral (blue) glomerular domains in the latent map defines the intra-hemispheric axis of symmetry (black line). Right: Medial and lateral sister glomeruli in 3D across left and right OB.

(f) Linear correlation between glomerular maps in the left and right OB across the medial-lateral (M-L), dorsal-ventral (D-V), and anterior-posterior (A-P) axes. Each dot represents a single glomerulus and is colored by glomerular domain. ρ = Pearson's correlation coefficient.

(g) Glomerular map showing the positions of 968 glomeruli expressing 255 OR genes. Glomeruli identified by the PGP model and obeying relative sister geometry defined by the AE model were included in the final map. Top panel shows the Z projection of the glomerular map, and bottom panel shows the Y projection.

(h) Linear correlation between rank of glomeruli in the ventromedial domain and predicted dorsolateral glomerular ranks. For details on glomerular ranking see Methods.

(i) Positions of the 968 lateral and medial glomeruli in latent space colored by medial glomerular rank.

(j) Linear correlation of pairwise distances between glomeruli in the left OB (x-axis) and right OB (y-axis). Color indicates the number of glomerular pairs.

Figure 4:

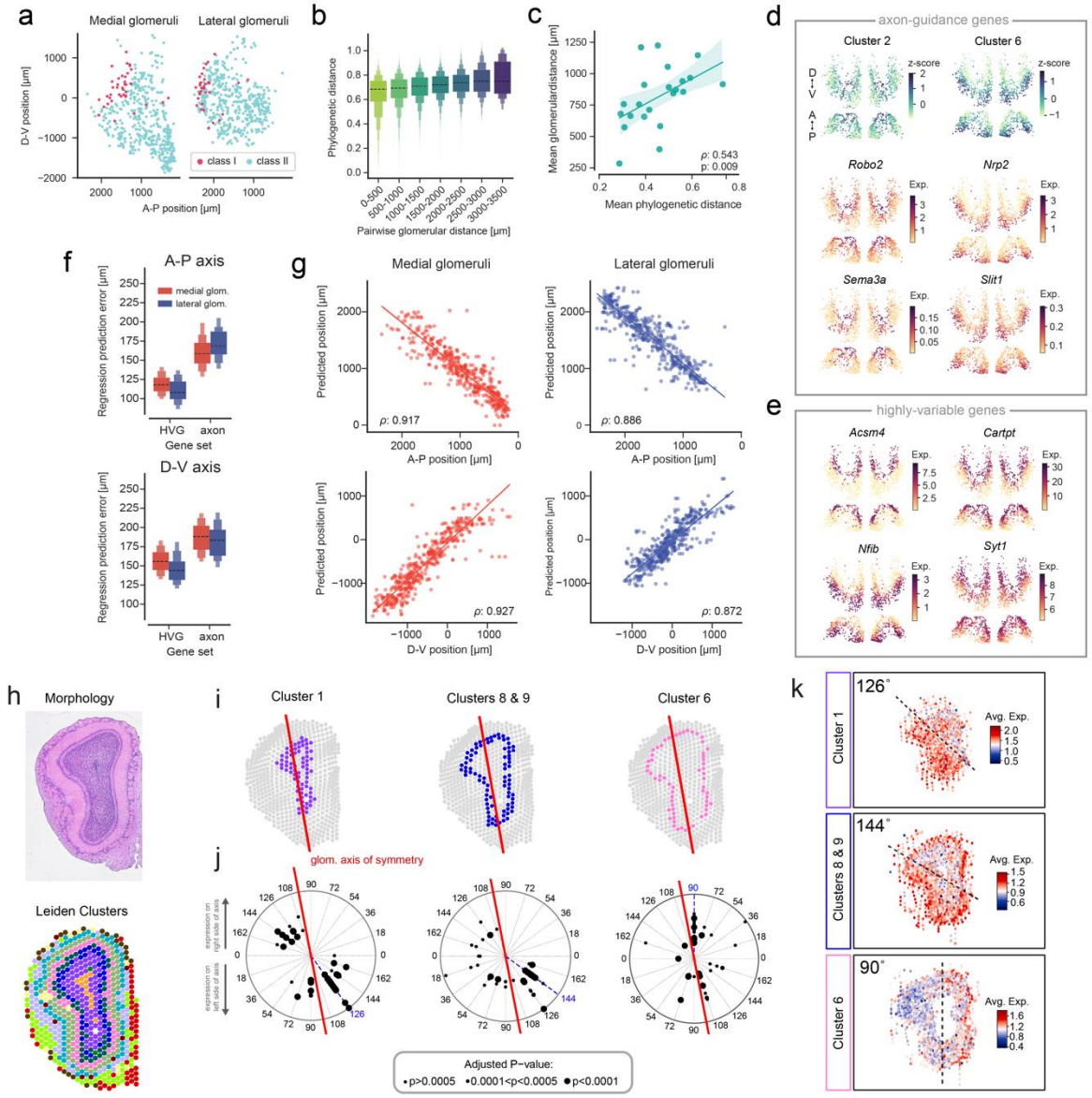
a
Medial glomeruli
Lateral glomeruli
D-V position [µm]
A-P position [µm]
class I
class II
b
Phylogenetic distance
Pairwise glomerular distance [µm]
c
Mean glomerulardistance [µm]
Mean phylogenetic distance
ρ: 0.543
p: 0.009
d
axon-guidance genes
Cluster 2
Cluster 6
z-score
Robo2
Nrp2
Sema3a
Slit1
Exp.
e
highly-variable genes
Acsm4
Cartpt
Nfib
Syt1
f
A-P axis
D-V axis
medial glom.
lateral glom.
Regression prediction error [µm]
HVG
axon
Gene set
g
Medial glomeruli
Lateral glomeruli
Predicted position [µm]
A-P position [µm]
D-V position [µm]
ρ: 0.917
ρ: 0.886
ρ: 0.927
ρ: 0.872
h
Morphology
Leiden Clusters
i
Cluster 1
Clusters 8 & 9
Cluster 6
j
glom. axis of symmetry
expression on right side of axis
expression on left side of axis
Adjusted P−value:
p>0.0005
0.0001<p<0.0005
p<0.0001
k
Cluster 1
Clusters 8 & 9
Cluster 6
126°
144°
90°
Avg. Exp.

Figure 4: OR identity and non-OR genes explain glomerular position

(a) Positions of glomeruli expressing Class I (magenta) and Class II (cyan) OR genes.

(b) Letter value boxplot of phylogenetic distance of ORs expressed in Class II glomeruli compared to pairwise glomerular distance (in μm), revealing that glomeruli expressing more phylogenetically similar Class II OR are located closer to each other in the OB.

(c) Correlation between mean phylogenetic distance and glomerular distance across chromosomal clusters (blue points).

(d) Top: Hierarchical clustering of axon guidance gene expression patterns revealed clusters that map onto the A-P (Cluster 2) and D-V (Cluster 6) axes of the OB. Bottom: Expression of individual axon guidance genes. Top plot shows Z-projection and bottom plot shows Y-projection of the OB

(e) Expression of individual highly variable genes. Top plot shows Z-projection and bottom plot shows Y-projection of the OB.

(f) Letter value boxplot of regression prediction error from elastic-net-regularized linear regression models trained on either a set of axon guidance genes or HVGs (highly variable genes) to predict glomerular positions. No significant difference exists between regression errors in predicting positions of glomeruli in the ventromedial or dorsolateral domains, but lower regression errors for HVGs indicate a higher accuracy in predicting glomerular positions based on this gene set.

(g) Correlations of predicted positions of glomeruli using a regression model trained on the HVG set. The model performed slightly better at predicting positions of medial glomeruli (red) across both the D-V and A-P axes (ρ=0.927 and 0.917, respectively) compared to lateral glomeruli (blue, ρ=0.872 and 0.886, respectively).

(h) Representative image of morphology (top) and capture spots in one section of the left OB with Leiden clusters (bottom).

(i) Capture spots in a single section colored by isolated Leiden cluster. Clusters isolated for analysis represent the deep granule cell layer (Cluster 1), superficial granule cell layer (Clusters 8 & 9), and mitral cell layer (Cluster 6). The glomerular axis of symmetry is overlaid in red.

(j) Polar plots showing the axis angle for the top 50 genes that maximize differential gene expression across the axis (see Methods). Red line is the glomerular axis. Genes on the top half of the polar plot are differentially expressed on the medial side of the axis and genes on the bottom half of the polar plot are differentially expressed on the lateral side of the axis. Size

of points represents the p-value of differential expression analysis, radius represents the log fold change.

(k) Expression signature of the peak axis angle within the isolated capture spots for each Leiden cluster flattened in 2D.

Figure S1:

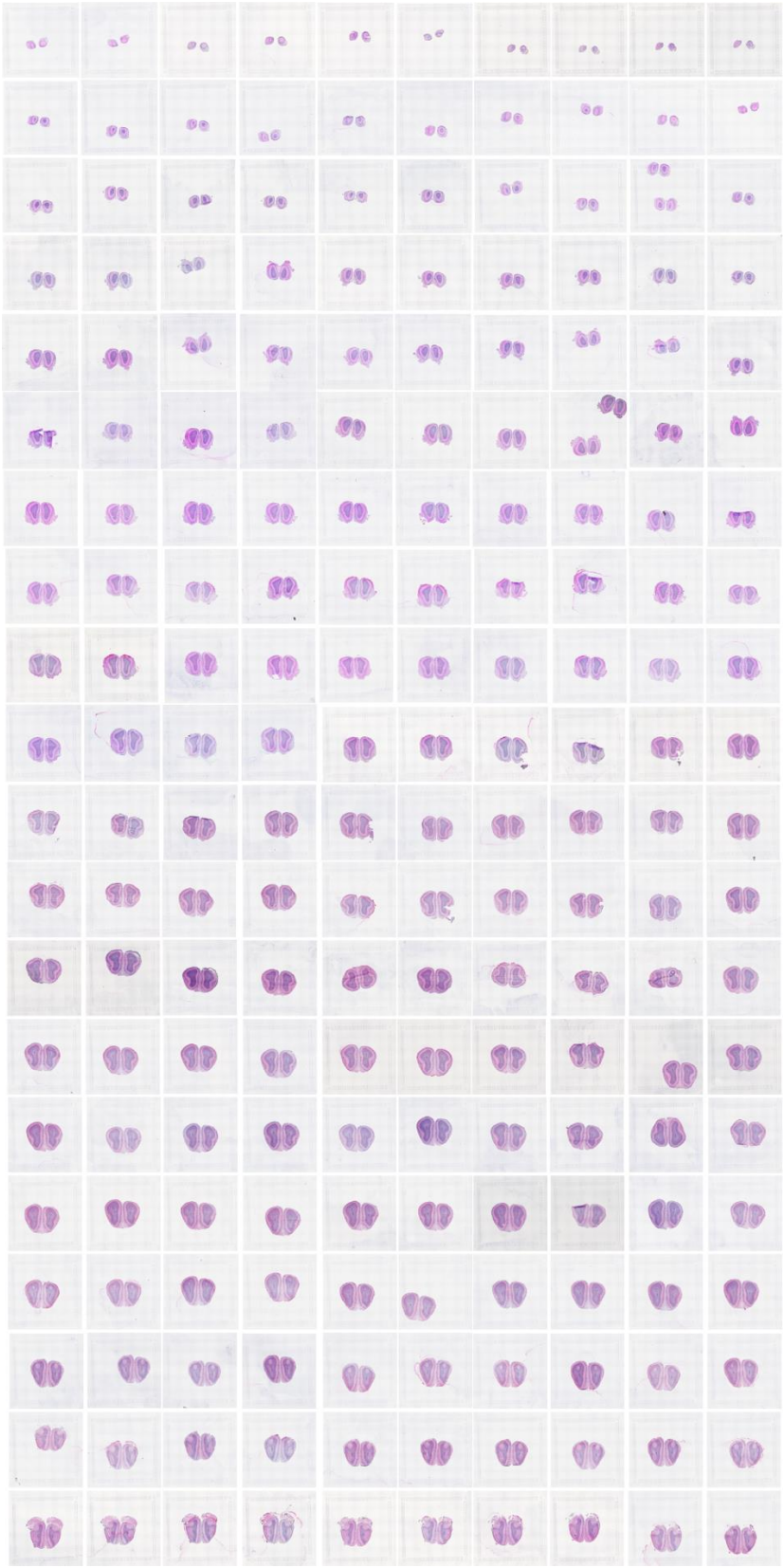

Figure S1: Morphology of the 200 consecutive sections of OB included in spatial transcriptomics dataset

(a) Brightfield images of OB tissue sections mounted onto spatial transcriptomics microarrays. Sections were stained with hematoxylin and eosin for alignment of morphology and gene expression data.

Figure S2:

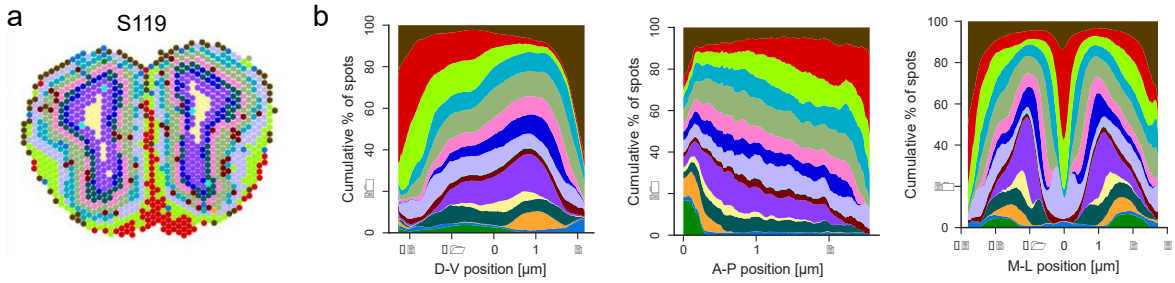

Figure S2: Leiden clustering of integrated capture spots across 200 sections

(a) Capture spots colored by Leiden cluster in section 119 out of 200 from the dataset.

(b) Cumulative distribution of capture spots across Leiden clusters across the entire dataset along the D-V, A-P, and M-L axis. Color indicates cluster identity. Values were binned and smoothed across the X, Y, and Z axes.

Figure S3:

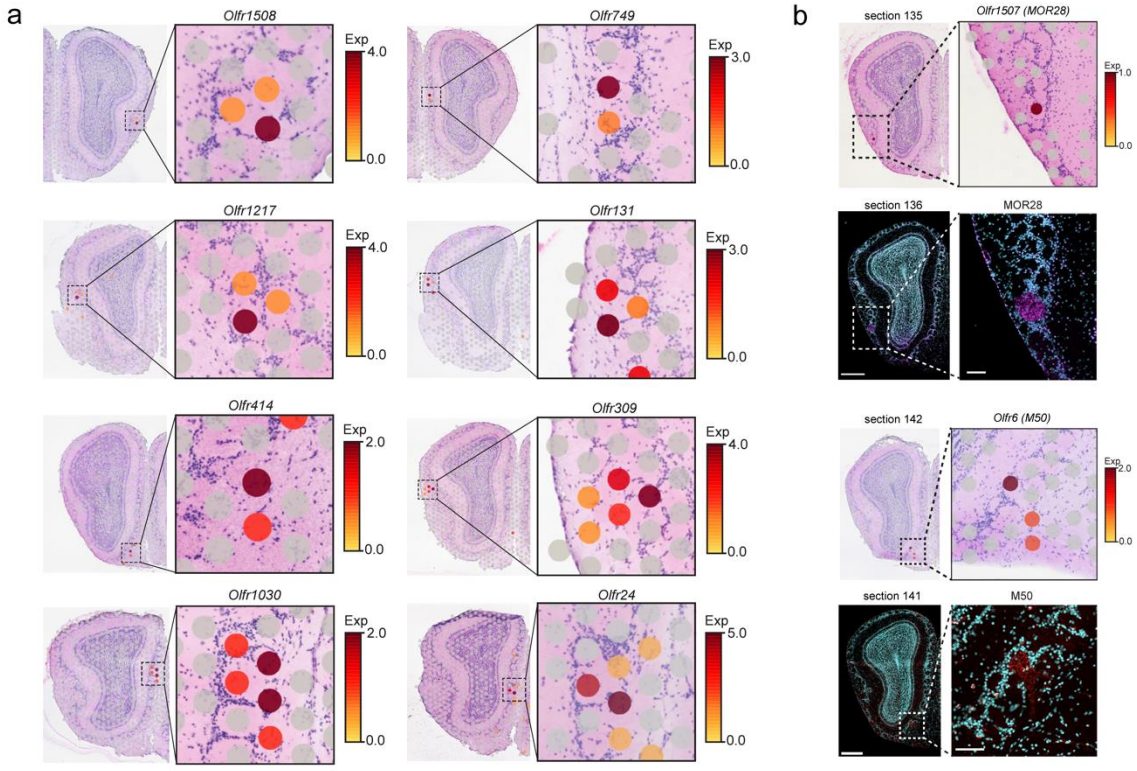

Figure S3: Odorant receptor expression in capture spots surrounding glomeruli

(a) Examples of gene expression of *Olfr1508*, *Olfr749*, *Olfr1217*, *Olfr131*, *Olfr414*, *Olfr309*, *Olfr1030*, and *Olfr24* in single tissue sections. High OR expression is restricted to 2-6 capture spots surrounding individual glomeruli.

(b) Validation of OR expression. Top: Capture of *Olfr1507* transcripts via spatial transcriptomics in section 135 aligns with targeting of MOR28 glomerulus (magenta) in section 136, localized via immunohistochemistry (see Methods). Bottom: Capture of *Olfr6* transcripts in section 142 aligns with targeting of M50 glomerulus (red) in section 141. DAPI in cyan. For top and bottom: Left scale bar = 500µm; right scale bar = 100µm.

Figure S4:

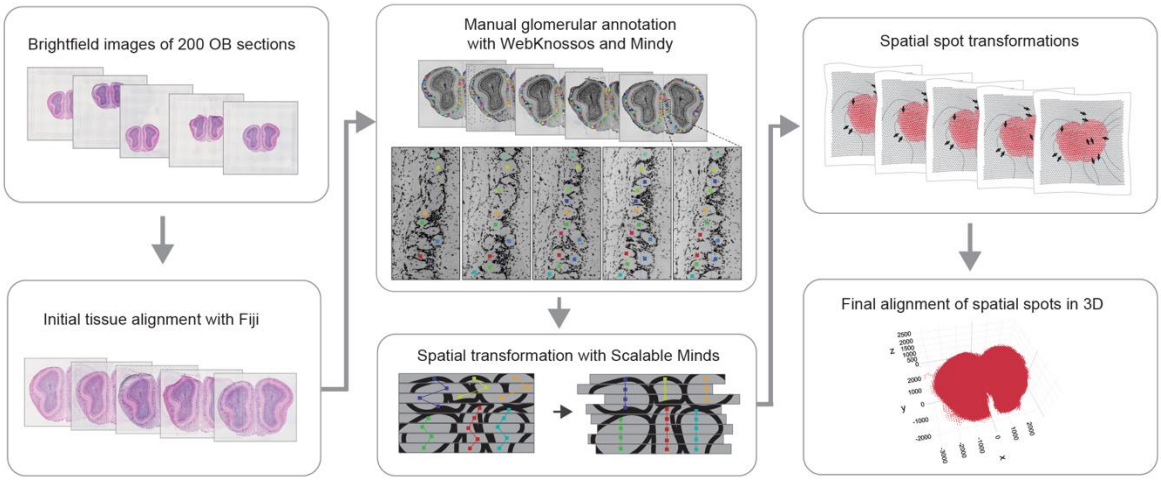

Figure S4: Morphological alignment of tissue sections to generate 3D map of OB

(a) The process of aligning spatial transcriptomics data from 200 consecutive OB sections involved the acquisition of brightfield images of OB sections stained with hematoxylin and eosin and initial tissue alignment of the sections with Fiji **(b)** (see Methods).

(c) Further refinement of the morphological alignment was then performed by annotating glomeruli, where individual glomeruli were identified across consecutive sections, using the nuclei of the periglomerular layer to distinguish glomeruli. Colored squares denote the centers of glomeruli that were tracked. Glomeruli were annotated using WebKnossos, and the annotation of over 2,500 glomeruli was performed using the annotation service Mindy.

(d) Spatial transformations were then performed with Scalable Minds to align sections based on the annotations.

(e) Finally, the spatial coordinates of the capture spots from the spatial transcriptomics data were transformed according to the morphological transformations, resulting in a final 3D plot of aligned capture spots from all 200 sections **(f)**.

Figure S5:

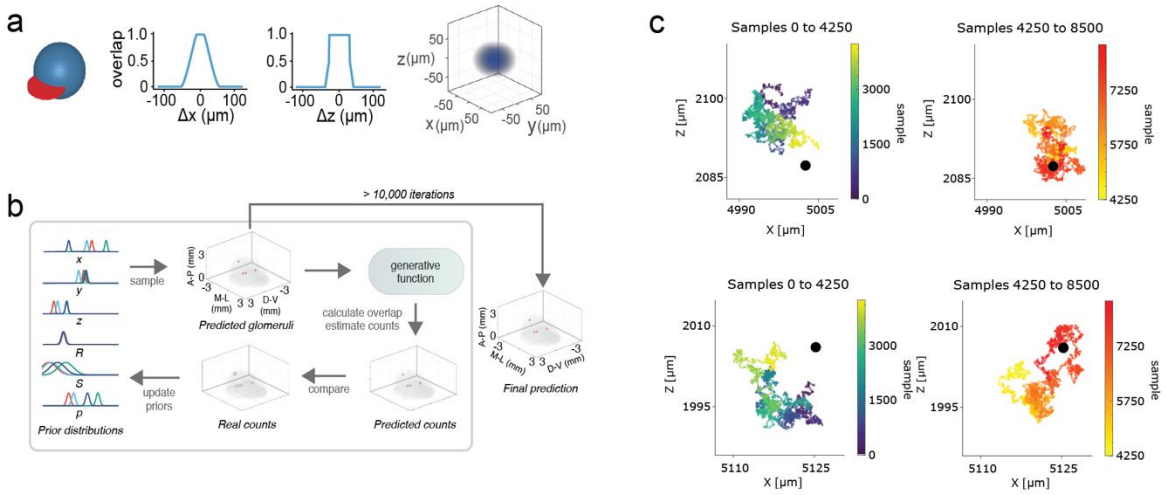

Figure S5: PGP model to predict centers of glomeruli from OR expression

(a) The generative function used by the PGP model. Count values at each spot depend on the overlap between the spherical glomerulus and the disk-shaped volume above the spot, resulting in a “squished ball” shaped distribution of count values around the glomerulus position (right).

(b) The MCMC algorithm performs probabilistic inference of glomerulus position (x, y, z), radius (R), strength (S), and probability of validity (p). Samples are drawn from the prior distributions to generate putative glomeruli. The generative function is used to estimate counts, which are compared with real counts to update priors iteratively. A final prediction of glomerular position is determined after greater than 10,000 iterations with 30 particles.

(c) Predicted glomerular position across successive iterations of MCMC algorithm for two different glomeruli. The predicted position of a glomerulus for iterations (‘Samples’) 0 to 4250 (Left) and iterations 4250 to 8500 (Right), with color in the plot indicating iteration. The black dot in both plots is the final predicted glomerular position.

Figure S6:

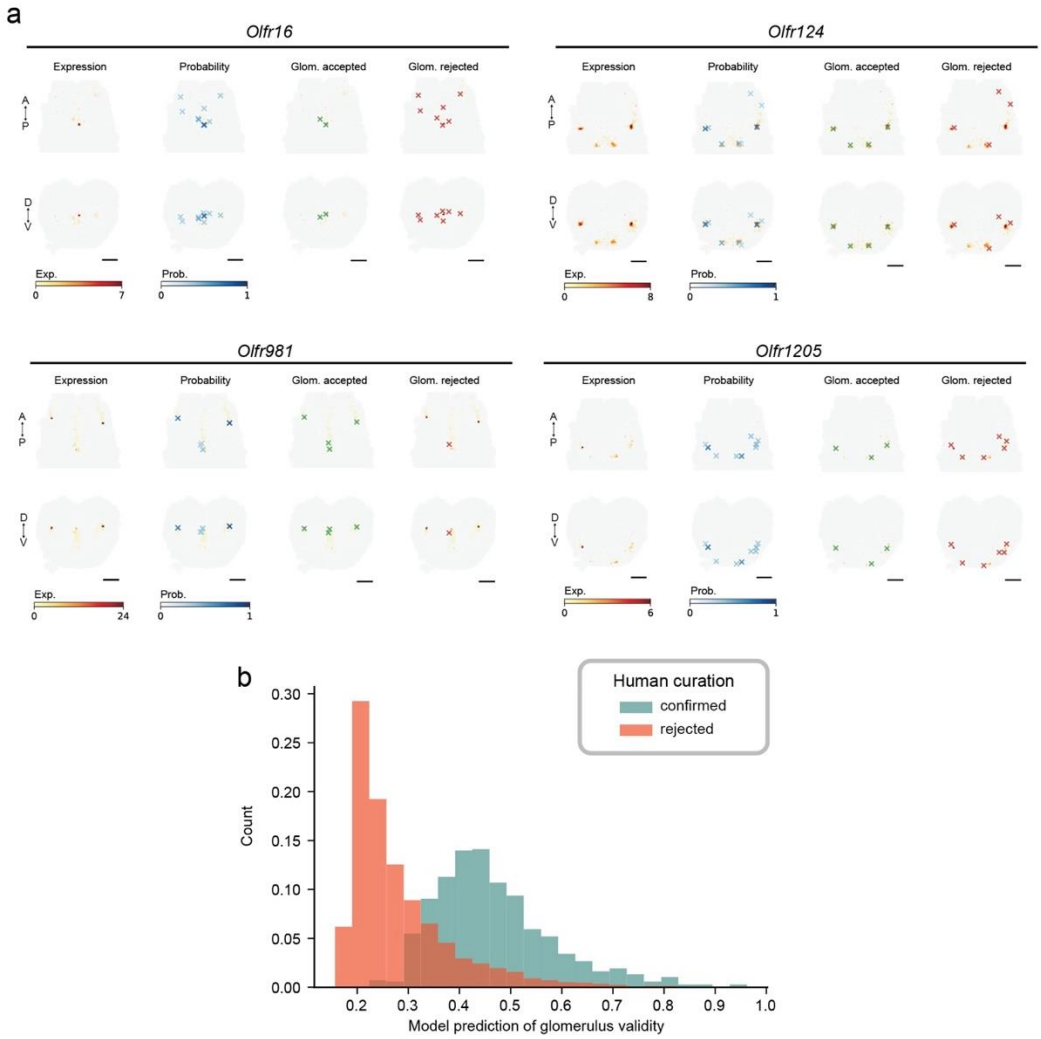

Figure S6: Human expert curation of glomerular positions output by PGP model

(a) Examples of accepted and rejected glomeruli for *Olfr16*, *Olfr124*, *Olfr981*, and *Olfr1205* after human curation. First column shows raw expression and second column shows glomerular positions output by the PGP model (Xs) colored by probability from 0 to 1. Third and fourth columns show positions accepted (green) or rejected (red) during expert curation.

(b) Comparison of model-generated probability values for glomerulus validity and human curation decisions. Confirmed glomeruli (green) and rejected glomeruli (red) showed good alignment with the model's goodness of fit for putative glomerular locations.

Figure S7:

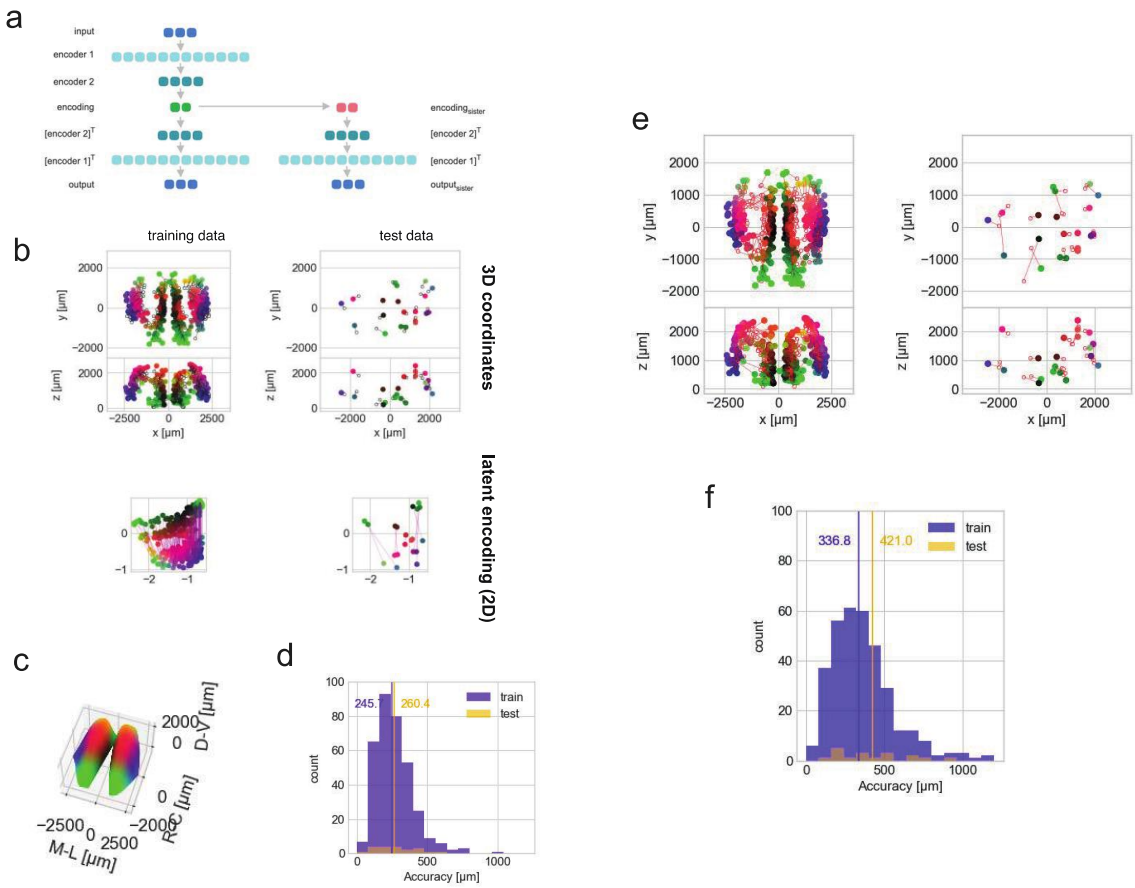
a
input
encoder 1
encoder 2
encoding
[encoder 2]T
[encoder 1]T
output
encoding_sister
[encoder 2]T
[encoder 1]T
output_sister
b
training data
test data
3D coordinates
latent encoding (2D)
y [µm]
z [µm]
x [µm]
c
D-V [µm]
R-C [µm]
M-L [µm]
d
train
test
count
Accuracy [µm]
e
y [µm]
z [µm]
x [µm]
f
336.8
421.0
train
test
count
Accuracy [µm]

Figure S7: Dual autoencoder model for mapping glomeruli and predicting sister glomerulus locations

(a) Architecture of the dual autoencoder model. After symmetrization, the glomerular coordinates are encoded through two encoder layers into a two-dimensional latent representation. The latent representation is decoded via the transposition of the same autoencoder layers to reconstruct the original data. A second branch of the model predicts the encoded location of sister glomeruli with a linear layer from the encoded glomerular location. Sister glomeruli are decoded with the same layers into 3D coordinates.

(b) Results after training of the dual autoencoder. Filled circles represent the original coordinates, and the linked open circles represent the corresponding reconstructed position. The color code is identical between the original coordinate plot (top) and the 2D latent map (bottom). On the latent map, sister glomeruli are shown as magenta lines.

(c) The 3D manifold learned by the autoencoder, showing 3D locations corresponding to each part of the latent space.

(d) Reconstruction precision after encoding and decoding. The lines represent mean precision for train and test data.

(e) 3D locations of test and train data for sister glomerulus prediction.

(f) Predictive accuracy of sister glomerulus precision of the dual autoencoder. Sister glomerulus locations can be predicted up to 421µm on previously unseen data, defining an upper bound for the precision of the glomerular map.

Figure S8:

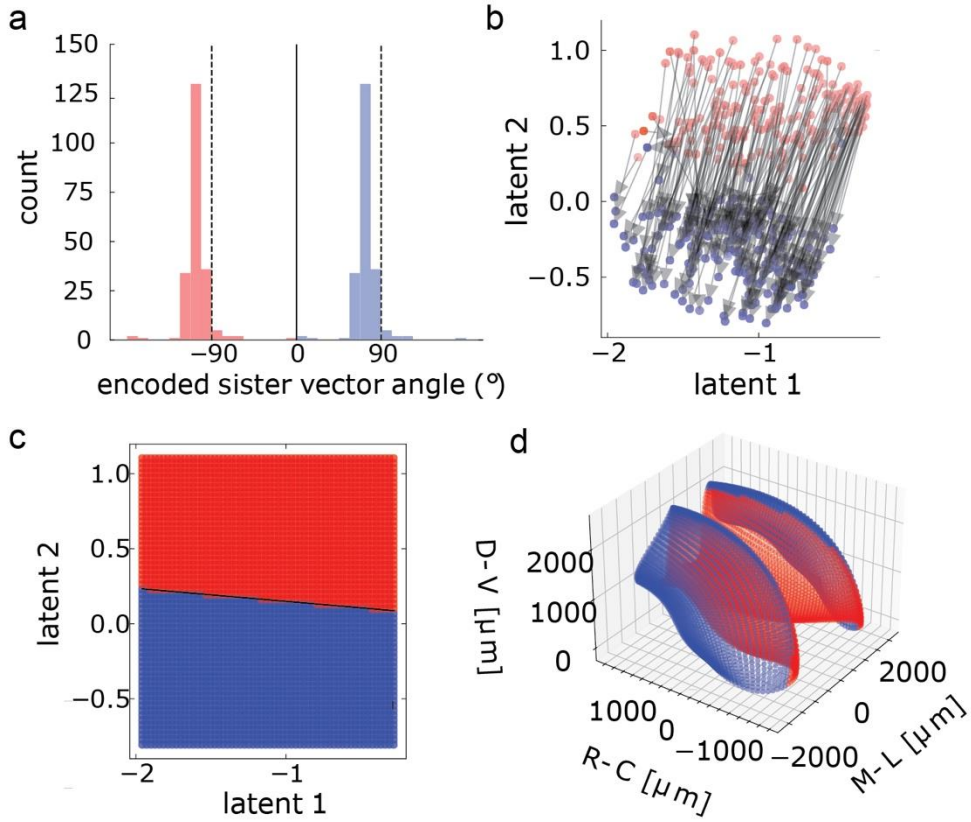

Figure S8: Classifying lateral and medial glomerular domains based on the relative location of sister glomeruli

(a) In the encoded map, the relative vector angles of sister glomeruli are well separated into two clusters.

(b) Glomeruli within the cluster of red sister glomeruli share similar vector direction and are spatially well separated from blue sister glomeruli in the encoded latent representation.

(c) The linear discriminant allows assigning any location in the glomerular manifold to either of the two glomerular domains.

(d) 3D Glomerular manifold with spots colored by domain identity in latent space.

Figure S9:

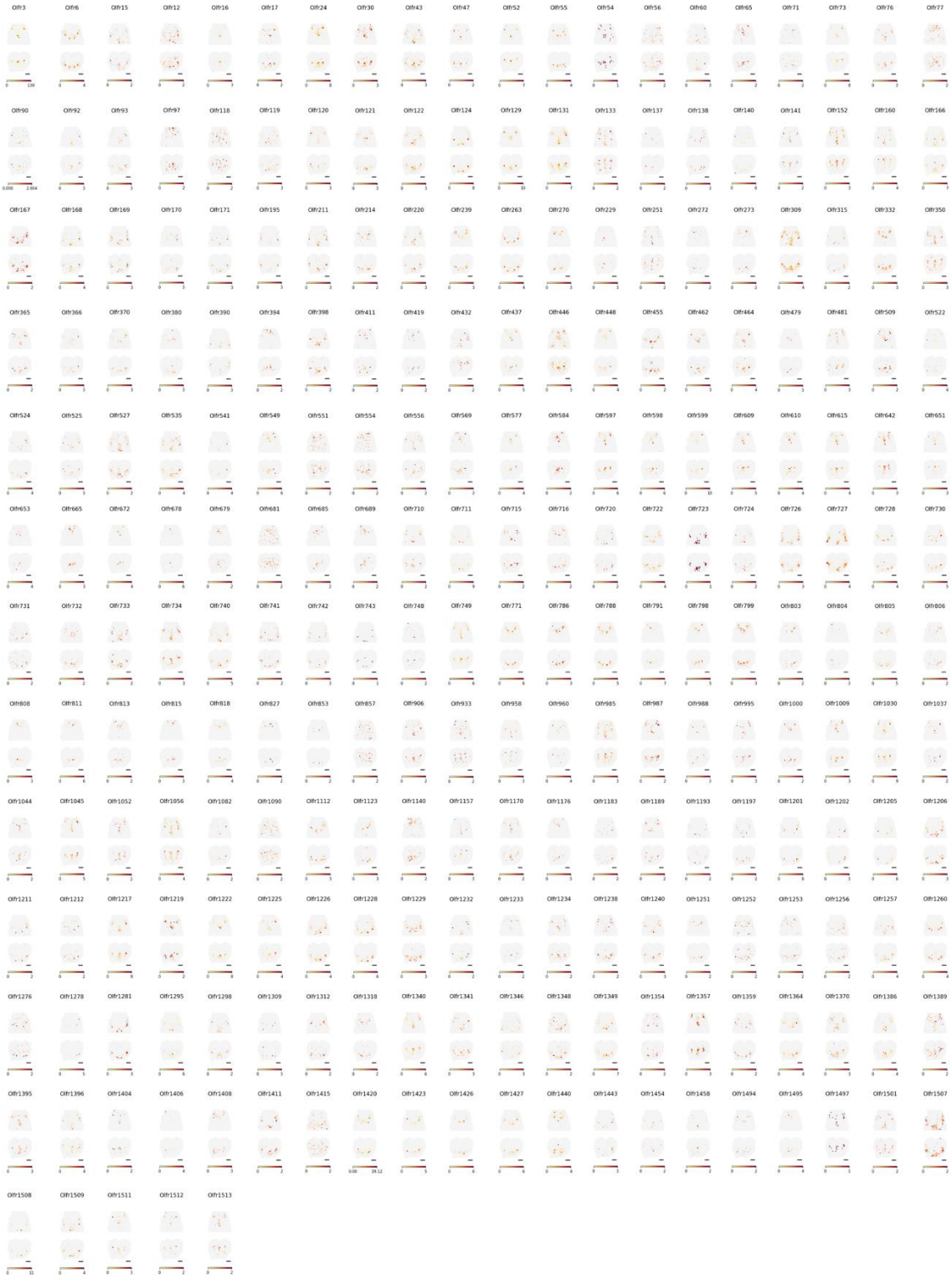
Olfr3
Olfr6
Olfr15
Olfr12
Olfr16
Olfr17
Olfr24
Olfr30
Olfr43
Olfr47
Olfr52
Olfr55
Olfr54
Olfr56
Olfr60
Olfr65
Olfr71
Olfr73
Olfr76
Olfr77
Olfr90
Olfr92
Olfr93
Olfr97
Olfr118
Olfr119
Olfr120
Olfr121
Olfr122
Olfr124
Olfr129
Olfr131
Olfr133
Olfr137
Olfr138
Olfr140
Olfr141
Olfr152
Olfr160
Olfr166
Olfr167
Olfr168
Olfr169
Olfr170
Olfr171
Olfr195
Olfr211
Olfr214
Olfr220
Olfr239
Olfr263
Olfr270
Olfr229
Olfr251
Olfr272
Olfr273
Olfr309
Olfr315
Olfr332
Olfr350
Olfr365
Olfr366
Olfr370
Olfr380
Olfr390
Olfr394
Olfr398
Olfr411
Olfr419
Olfr432
Olfr437
Olfr446
Olfr448
Olfr455
Olfr462
Olfr464
Olfr479
Olfr481
Olfr509
Olfr522
Olfr524
Olfr525
Olfr527
Olfr535
Olfr541
Olfr549
Olfr551
Olfr554
Olfr556
Olfr569
Olfr577
Olfr584
Olfr597
Olfr598
Olfr599
Olfr609
Olfr610
Olfr615
Olfr642
Olfr651
Olfr653
Olfr665
Olfr672
Olfr678
Olfr679
Olfr681
Olfr685
Olfr689
Olfr710
Olfr711
Olfr715
Olfr716
Olfr720
Olfr722
Olfr723
Olfr724
Olfr726
Olfr727
Olfr728
Olfr730
Olfr731
Olfr732
Olfr733
Olfr734
Olfr740
Olfr741
Olfr742
Olfr743
Olfr748
Olfr749
Olfr771
Olfr786
Olfr788
Olfr791
Olfr798
Olfr799
Olfr803
Olfr804
Olfr805
Olfr806
Olfr808
Olfr811
Olfr813
Olfr815
Olfr818
Olfr827
Olfr853
Olfr857
Olfr906
Olfr933
Olfr958
Olfr960
Olfr985
Olfr987
Olfr988
Olfr995
Olfr1000
Olfr1009
Olfr1030
Olfr1037
Olfr1044
Olfr1045
Olfr1052
Olfr1056
Olfr1082
Olfr1090
Olfr1112
Olfr1123
Olfr1140
Olfr1157
Olfr1170
Olfr1176
Olfr1183
Olfr1189
Olfr1193
Olfr1197
Olfr1201
Olfr1202
Olfr1205
Olfr1206
Olfr1211
Olfr1212
Olfr1217
Olfr1219
Olfr1222
Olfr1225
Olfr1226
Olfr1228
Olfr1229
Olfr1232
Olfr1233
Olfr1234
Olfr1238
Olfr1240
Olfr1251
Olfr1252
Olfr1253
Olfr1256
Olfr1257
Olfr1260
Olfr1276
Olfr1278
Olfr1281
Olfr1295
Olfr1298
Olfr1309
Olfr1312
Olfr1318
Olfr1340
Olfr1341
Olfr1346
Olfr1348
Olfr1349
Olfr1354
Olfr1357
Olfr1359
Olfr1364
Olfr1370
Olfr1386
Olfr1389
Olfr1395
Olfr1396
Olfr1404
Olfr1406
Olfr1408
Olfr1411
Olfr1415
Olfr1420
Olfr1423
Olfr1426
Olfr1427
Olfr1440
Olfr1443
Olfr1454
Olfr1458
Olfr1494
Olfr1495
Olfr1497
Olfr1501
Olfr1507
Olfr1508
Olfr1509
Olfr1511
Olfr1512
Olfr1513

Figure S9: Expression of OR genes included in the final dataset of 968 glomeruli

Raw expression of 255 OR genes, visualized as a maximum Z-projection (top) and Y-projection (bottom).

Figure S10:

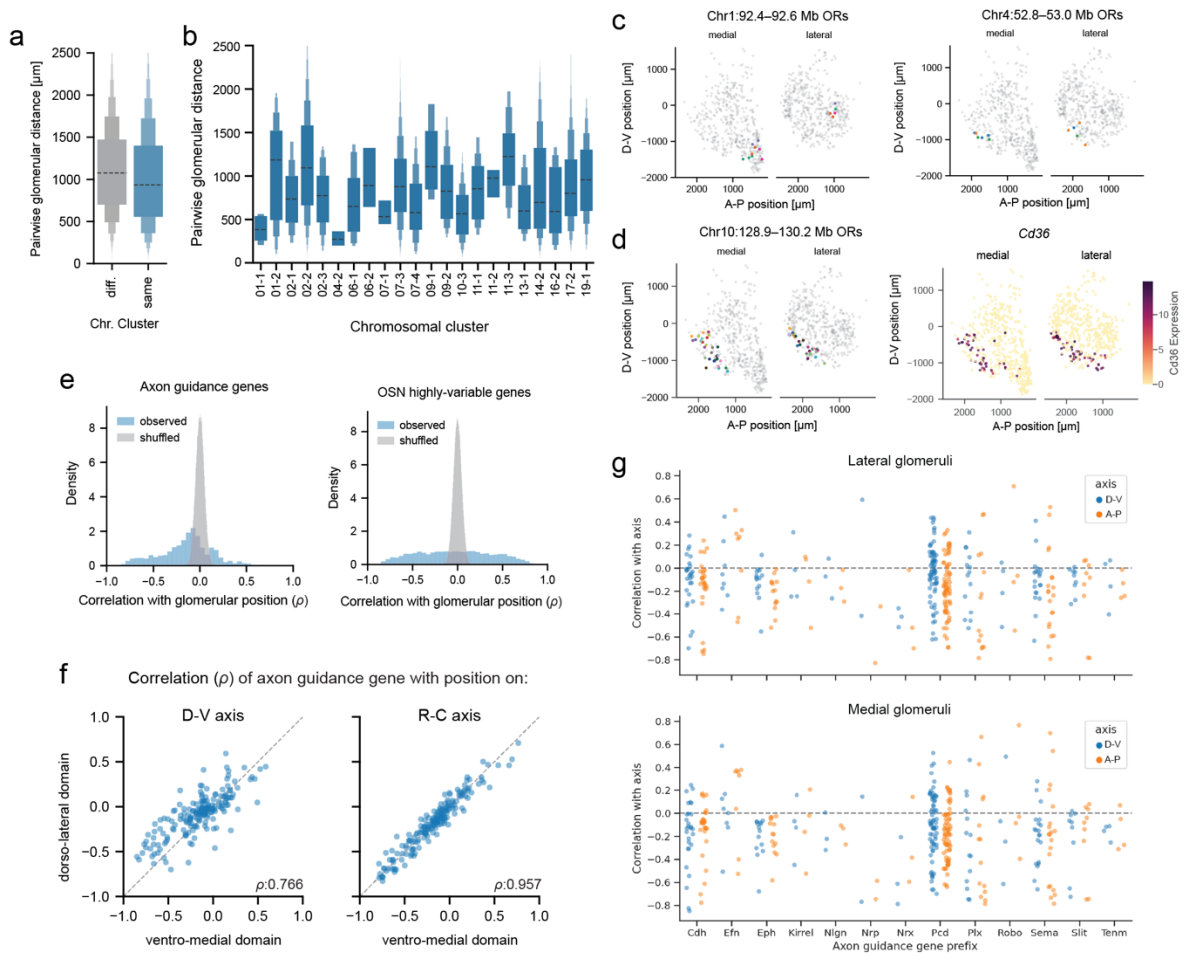
a
Pairwise glomerular distance [µm]
diff.
same
Chr. Cluster
b
Pairwise glomerular distance
Chromosomal cluster
c
Chr1:92.4–92.6 Mb ORs
Chr4:52.8–53.0 Mb ORs
medial
lateral
D-V position [µm]
A-P position [µm]
d
Chr10:128.9–130.2 Mb ORs
Cd36
Cd36 Expression
e
Axon guidance genes
OSN highly-variable genes
observed
shuffled
Density
Correlation with glomerular position (ρ)
f
Correlation (ρ) of axon guidance gene with position on:
D-V axis
R-C axis
dorso-lateral domain
ventro-medial domain
ρ:0.766
ρ:0.957
g
Lateral glomeruli
Medial glomeruli
axis
D-V
A-P
Correlation with axis
Cdh
Efn
Eph
Kirrel
Nlgn
Nrp
Nrx
Pcd
Plx
Robo
Sema
Slit
Tenm
Axon guidance gene prefix

Figure S10: OR identity and transcriptome-wide gene expression correlate with glomerular position

(a) Boxplot of pairwise glomerular distance for glomeruli expressing ORs on the same or different chromosomal cluster.

(b) Boxplot of pairwise glomerular distance for ORs in 22 chromosomal clusters.

(c) Spatial position of glomeruli expressing ORs in chromosome 1:92.4-92.6 Mb (left plot) and chromosome 4:52.8-53.0 Mb (right plot), showing that glomeruli expressing these ORs are located close together in the OB.

(d) Spatial position of glomeruli expressing ORs in chromosome 10:128.9-130.2 Mb (left plot) and expression of *Cd36* (right plot) show a high correlation.

(e) Histograms of observed correlation with glomerular position for axon guidance genes (left) and highly variable genes (right plot) versus shuffled control.

(f) Correlations of predicted positions of glomeruli using a regression model trained on the axon guidance gene set. The model performed better at predicting positions of glomeruli across the R-C axiDs than the D-V axis (ρ=0.957 and 0.766, respectively).

(g) Dotplot of gene correlation with the D-V axis (blue) or A-P axis (orange) for individual axon guidance genes. Top plot shows correlations for lateral glomeruli and bottom plot shows correlations for medial glomeruli.

Figure S11:

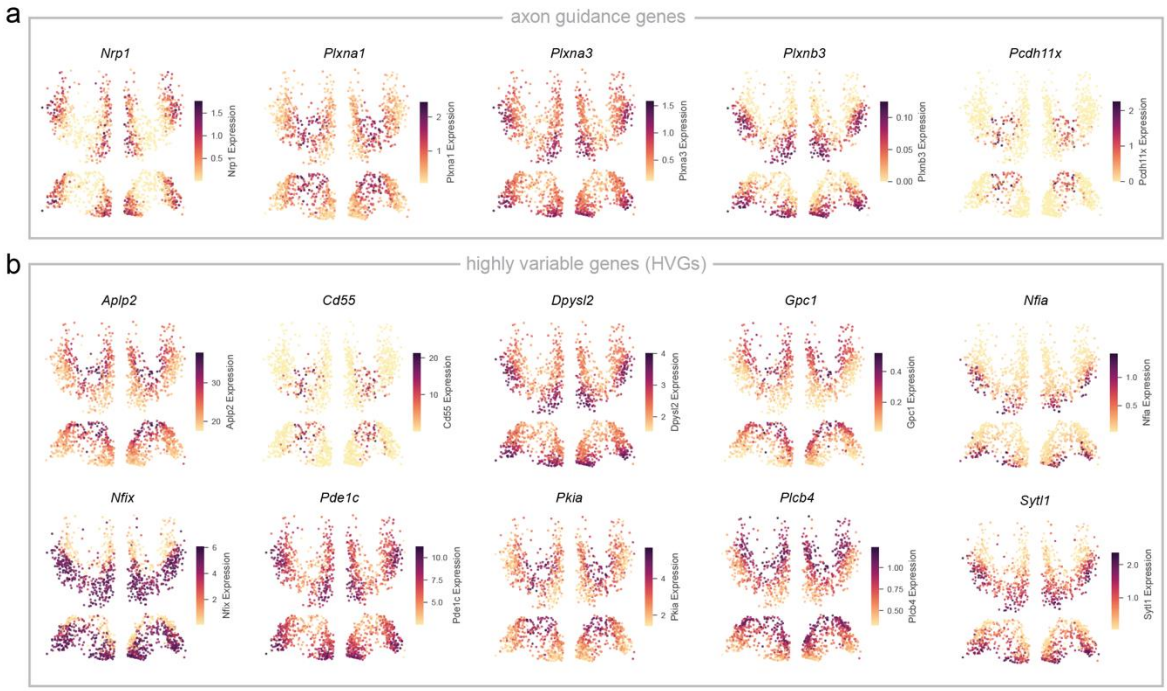

Figure S11: Additional expression examples of axon guidance genes and HVGs

(a) Expression of individual axon guidance genes *Nrp1*, *Plxna1*, *Plxna3*, *Plxnb3*, and *Pcdh11x* the in glomerular map. The top plot shows Z-projection and bottom plot shows Y-projection of the OB.

(b) Expression of highly variable genes *Aplp2*, *Cd55*, *Dpsyl2*, *Gpc1*, *Nfia*, Nfix, *Pde1c*, *Pkia*, *Plcb4*, and *Sytl1* in the glomerular map. Top plot shows Z-projection and bottom plot shows Y-projection of the OB.

METHODS

Experimental model and subject details

One male WT C57Bl/6 mouse (7-weeks old) was used in this study and obtained from Jackson Laboratories. All animal protocols were approved by the Brown University's Institutional Animal Care and Use Committee (protocol number: 21-03-0004) followed by the guidelines provided by the National Institutes of Health.

Spatial transcriptomics of mouse olfactory bulb

Tissue dissection and sectioning

Whole olfactory bulb tissue was dissected, embedded in OCT and frozen in a bath of 2-methylbutane surrounded by powdered dry ice. 200 consecutive 10µm sections of tissue were sectioned on a Leica CM3050 S cryostat, mounted onto Visium Spatial Gene Expression slides (10X Genomics) and maintained at -80˚C until processing. Every fifth 10 µm cryosection was mounted onto a standard Superfrost microscope slide (Fisher Scientific) and saved at -80˚C to use for OR expression validation using immunohistochemistry with OR antibodies against *Olfr6* (M50) and *Olfr1507* (MOR28). A small set of tissue sections (17) were not mounted on Visium slides or standard microscope slides due to damage. These sections were accounted for as 10µm 'gaps' in the alignment of the 3D OB dataset.

Fixation, staining, and imaging of tissue sections

The 200 sections were processed according to the Visium Spatial Gene Expression with slight modifications. Prior to the experiment, a preliminary tissue optimization experiment was performed to determine the minimum tissue permeabilization time to yield high capture of OR mRNA from delicate OSN axon termini. Tissue sections from 4 Visium slides (16 sections total) were processed each day. Slides were removed from -80˚C, tissue sections were dried by incubating on a thermal cycler at 37˚C for 1 minute, and were then fixed in methanol for 30 minutes in -20˚C. The sections were then stained with Hematoxylin and Eosin according to the 10X Visium protocol and imaged using a Nikon Eclipse Ti2 inverted microscope to obtain reference histology images for each tissue section.

Tissue sections were then permeabilized for 6 minutes according to the preliminary optimization experiment, allowing for mRNA to diffuse and be captured by barcoded mRNA capture probes printed on the Visium slides. The captured mRNA transcripts were then reverse-transcribed, and second-strand cDNA was generated. Then, qPCR was performed to determine C_t values for each sample, and PCR amplification was performed on the samples.

Barcoded cDNA libraries of the 200 tissue sections were generated using the Spatial Gene Expression reagents (10X Genomics) according to the manufacturer's protocols. Libraries

were pooled and sequenced on an Illumina NovaSeq instrument using the following run variables: 28 cycles (Read 1); 10 cycles (i7 index); 10 cycles (i5 index); 120 cycles (Read 2). The samples were initially sequenced to achieve an average depth of 50,000 read pairs per capture spot, then sequenced again to achieve a final average depth of 200,000 read pairs per capture spot.

Data pre-processing

Data were demultiplexed and processed using SpaceRanger v1.1.0. For quality control checks of non-OR gene expression in the OB, reads were aligned to the mouse genome (mm9). The reads were pseudoaligned to the mouse transcriptome using the alevin-fry pipeline to account for the highly homologous sequences of OR genes[63].

Visualization of gene expression in individual sections

Analysis of spatial transcriptomics data in individual tissue sections was performed in R using Seurat V4. Expression data was normalized using SCTransform where indicated and expression of individual genes (layer marker genes and OR genes) was overlaid against H&E histology images. For the identification of glomerulus positions, raw (non-normalized) and non-filtered data of OR gene expression were used due to the highly variable and sparse capture of OR genes.

Integration of capture spots and deconvolution with scRNA-seq OB dataset

Gene expression from 190,445 capture spots across the 200 spatial transcriptomics datasets was integrated using the scVI analysis pipeline from scvi-tools. The clustering of capture spots was performed using the Leiden algorithm, producing 16 clusters.

Deconvolution and visualization of the integrated spatial transcriptomics dataset was performed using Deconvolution of Spatial Transcriptomics profiles using Variational Inference (DestVI) from scvi-tools. The single-cell model (scLVM) was trained using an integrated OB scRNA-seq dataset[25,64], and then the spatial model (stLVM) was trained to perform the deconvolution.

Immunohistochemistry to validate OR transcript capture

10µm tissue sections saved in -80˚C for validation were first dried for 1 min at 37˚C and fixed for 7 min in 2% PFA. Sections were washed in PBS three times for 10 min, permeabilized in PBS and 0.1% Triton X-100 for 30 min, then blocked in PBS, 0.1% Triton X-100 and 5% heat-inactivated horse serum at room temperature for 30 min. Sections were then incubated overnight at 4˚C with primary antibodies against M50 (guinea pig, 1/1000, Gilad Barnea) and MOR28 (rabbit, 1/1000, Gilad Barnea). Sections were then washed with PBS and 0.1% Triton X-100 three times for 10 min, blocked in PBS, 0.1% Triton X-100 and 5% heat-inactivated

horse serum at room temperature for 30 min, then incubated with secondary antibodies, anti-guinea pig conjugated to 488 and anti-rabbit conjugated to Cy3 (1/1000, Donkey IgG (H+L), Jackson ImmunoResearch) for 2 hours at room temperature in the dark. Sections were rinsed three times with PBS and 0.1% Triton X-100 and sealed with Fluorescent Vectashield Mounting Medium (Vector, H-1900), and imaged at 20X using a Nikon A1R0HD confocal microscope.

Three-dimensional alignment of morphology and gene expression

Manual annotation and alignment of morphological sections

Manual annotation was necessary to account for stretching, folding, and damage of tissue sections during mounting. Initial alignment was performed by first conducting coarse alignment through grey-level thresholding to identify tissue areas, followed by cropping a square region centered on the centroid of the segmented object. Misaligned tissue sections were manually corrected by flipping them horizontally or vertically as needed. Subsequently, a custom FIJI script[65] was employed to align the image stack using BUnwarpJ[66], an elastic registration tool. Finally, the transformations generated by BUnwarpJ were applied to the corresponding spot coordinates.

Further refinement was performed via manual annotation of glomeruli using WebKnossos and the data annotation service Mindy[67]. First, based on the distribution of nuclei in the reference histology images, the centers of 2,550 glomeruli were annotated in individual sections across the 200 tissue sections. Then, glomeruli were annotated by identifying the centers of the same glomeruli across consecutive sections. The resulting glomerular annotations were then used to refine the morphological alignment using AI computer vision with Scalable Minds, by performing fine-scale spatial transformations of the tissue sections.

Alignment of gene expression data in 3D

The gene expression data was aligned in 3D according to the morphological alignment, by transforming the capture spot position of the gene expression data to the aligned morphological images. The z-position for the 3D dataset was approximated based on the thickness of tissue sections (10μm).

Computational modeling to quantify glomerular position

Probabilistic Glomerulus Position (PGP) Model

To identify the precise locations of olfactory glomeruli from the spatial transcriptomics data, we developed a model that predicts the expected gene counts at each spot based on the positions and radii of putative glomeruli. The model assumes that the count value at a spot is proportional to the overlap between the spot's surface (modelled as a disk) and the glomerulus

(modelled as a sphere). We define the overlap function $O(R_g, \Delta x, \Delta y, \Delta z)$ that calculates the proportion of the spot area occupied by a glomerulus with radius R_g, $\Delta x, \Delta y$ and Δz representing the distances between the spot and glomerulus centres in the x, y, and z directions, respectively. The overlap function is given by:

$$O(R_g, \Delta x, \Delta y, \Delta z) = \frac{f_1 + f_2 - f_3}{R_s^2 \cdot \pi}$$

where R_s is the spot radius, and f_1, f_2 and f_3 are calculated as follows:

$$R_\chi = \sqrt{{R_g}^2 - \Delta z^2}$$

(The radius of the circular cross-section of the glomerulus in the plane of the spot.)

$$d = \sqrt{\Delta x^2 + \Delta y^2}$$

$$d_1 = \frac{R_s^2 - R_\chi^2 + d^2}{2 \cdot d}$$

$$d_2 = \frac{R_\chi^2 - R_s^2 + d^2}{2 \cdot d}$$

$$f_1 = R_s^2 \cdot cos^{-1}\left(\frac{d_1}{R_s}\right) - d_1 \cdot \sqrt{R_s^2 - d_1^2}$$

$$f_2 = R_\chi^2 \cdot cos^{-1}\left(\frac{d_2}{R_\chi}\right)$$

$$f_3 = d_2 \cdot \sqrt{R_\chi^2 - d_2^2}$$

The count value C_n at spot n is pulled from a normal distribution (allowing for non-integer count values) with a mean determined by the sum of overlaps with all K glomeruli, their respective expression strengths S and the binary variable $V \in \{0,1\}$ representing the validity of the glomerulus (whether it should be considered), calculated from a glomerulus validity probability value $V = Bernoulli(p)$).

$$C_n \sim \mathcal{N}\left(\sum_{k=1}^{K} S_k \cdot O(R_g, \Delta x, \Delta y, \Delta z) \cdot V_k\right)$$

The above functions were implemented in Julia (version 1.9.2). Probabilistic modeling and inference were performed using Turing.jl (version 0.28.2). The model parameters, including glomerulus centers (x, y, z) and validity probabilities p, are inferred using a particle Markov chain Monte Carlo (MCMC) algorithm.

Prior putative glomerular locations were initialized for optimal computational efficiency based on the raw spot count values by a lenient heuristic method. Initial peaks in the gene expression data were identified by comparing the expression values to a detection threshold (20% of the mean expression value). To determine the strength value of each glomerulus for the prior distribution, the overlap function $O(R_g, \Delta x, \Delta y, \Delta z)$ was used (for the heuristic function) to update the count value of each spot based on their distance from neighboring spots and their count values. Peaks with expression levels below 0.2 were discarded, and all other peaks were clustered based on their Euclidean distance. The median coordinates of peak clusters within 100 μm were used as the expected value of glomerular centers, and the maximal peak expression value of the spots within the cluster was used as the estimated strength value. Priors were defined for the center coordinates as normal distributions with a 200 μm standard deviation, and the mean was defined by the heuristic described above. Log-normal priors were used for the radii (50 μm expected value) and strength (as defined by the heuristic function). For the glomerulus probability, a Kumaraswamy distribution was used (instead of a Beta distribution to improve computational efficiency), with a variance of 0.1 and expected value based on the relative strength of the glomerulus compared to the maximal count value in the gene's dataset ($\frac{S}{\max(S)}$)

The probabilistic model was sampled for 10,000 iterations for each gene with a particle Gibbs sampler using 30 particles in parallel.

Human Expert Curation of High-Confidence Glomeruli

The curated dataset was generated by simultaneously displaying the entire raw dataset for each gene in an interactive navigable 3D plot together with the proposed glomeruli and their overlap. Each putative glomerulus was confirmed if the glomerular signal was clearly visible at the center of the putative glomerulus and not associated with afferent axonal fibers or background.

Symmetrization of Left and Right Hemi-Bulbs

First, manually curated divider points separating the left and right bulbs were annotated in WebKnossos [3]. A curved divider surface was fitted to the divider points using a dense mesh grid (L-BFGS-B minimization algorithm). All glomeruli in the output of the PGP model were assigned *right* or *left* laterality according to their position relative to the divider surface. For

symmetrization, a cost function was defined to measure the dissimilarity between the positions of glomeruli in the left and right bulbs after applying a transformation. Deviations from symmetry were minimized using the L-BFGS-B algorithm to find the optimal symmetrization vector that aligns the glomeruli in the left and right bulbs. The glomeruli positions in the right olfactory bulb were transformed using the estimated symmetrization vector. The transformed right glomeruli positions were concatenated with the original left ones to create a symmetrized dataset.

Double Autoencoder (AE) Model for Sister Glomerulus Positions

To model the relative positions of sister glomeruli in the medial and lateral domains of the olfactory bulb, we developed a dual autoencoder architecture consisting of a two-layer encoder network and two decoder networks. The model aims to:

1) Map the 3D positions of glomeruli onto a 2D latent space (embedding) from which it can reliably reconstruct the original positions. 2) Predict the position of the sister glomerulus for each glomerulus. 3) Ensure that the mapping of glomeruli and sister glomeruli are similar in the latent space.

The dual autoencoder model was designed with minimal trainable parameters to allow generalization on the curated glomerulus dataset. It consists of the following components:

<u>Encoder:</u> A two-layer (21 and 7 neurons) dense neural network that maps the 3D glomeruli positions to a lower-dimensional latent space. The encoder layers use sigmoid activation function and L2 regularization.

<u>Decoder:</u> A two-layer dense neural network that reconstructs the 3D glomeruli positions from the latent space representation. The decoder layers are tied to the encoder layers, sharing the same architecture and weights.

<u>Sister Glomerulus Predictor:</u> A single dense layer with linear activation that predicts the latent space representation of the sister glomerulus given the latent space representation of a glomerulus.

<u>Sister Glomerulus Decoder:</u> A decoder network that reconstructs the 3D position of the sister glomerulus from its predicted latent space representation. It is identical to the main Decoder and shares the same weights.

The dual autoencoder model is trained using a compound loss function combining:

<u>Reconstruction Loss:</u> Mean squared error (MSE) between the input 3D glomeruli positions and their reconstructed positions from the autoencoder.

Sister Glomerulus Prediction Loss: MSE between the predicted 3D positions of sister glomeruli and their true positions.

Encoding Similarity Loss: MSE between the predicted latent space representation of the sister glomerulus (from the Sister Glomerulus Predictor) and its encoding from tissue coordinates (from the Encoder).

The resulting latent space representation can reveal clusters or patterns related to the medial and lateral domains of the olfactory bulb, allowing for unsupervised assignment of medial/lateral labels to each glomerulus based on their relative positions to their sisters. The trained dual autoencoder model can be used for various tasks, such as: Encoding glomeruli positions to the latent space, decoding latent space representations to reconstruct glomeruli positions, predicting the positions of sister glomeruli given a glomerulus position, and inferring the medial/lateral labels of glomeruli based on their relative latent space representations.

Confirmation of Glomeruli using PGP and AE Model Predictions

To confirm the validity of the glomeruli identified by the PGP model, and identify the most likely set of glomeruli for each gene, we utilized the predictions from the AE model. The confirmation process was performed using the following steps:

Each gene's dataset was separately analyzed. Mirror positions of the glomeruli were calculated by negating the x-coordinate of the left glomeruli and assigning it to the right glomeruli after symmetrization. The Euclidean distances between the mirror positions of the left and right glomeruli were calculated. These distances represent the mirror errors, indicating how well the putative glomeruli align with their mirror counterparts. The dual autoencoder model was used to predict the positions of the sister glomeruli for each putative glomerulus. The Euclidean distances between the predicted putative sister positions and the actual glomeruli positions were calculated. These distances represent the sister errors, indicating how well glomeruli aligned with the predicted other glomeruli on the same side.

Glomeruli were considered valid if they satisfied the following criteria:

1) Either the sister error or the mirror error was less than 250 microns. 2) The probability of the glomerulus, as predicted by the PGP model was greater than 0.25.

For each gene, combinations of valid glomeruli were exhaustively searched to find the combination with the minimum total error, considering both sister errors and mirror errors. The search started with combinations of 4 glomeruli and decreased to 2 glomeruli if a satisfactory combination was not found.

Ranking sister glomeruli

Medial geometrically-confirmed glomeruli were ranked along a single axis using a nearest-neighbor approach. 3-D glomerular positions were scaled using scikit-learn's RobustScaler, and a k-nearest neighbor graph was constructed using k=10 neighbors. To obtain a stable ranking of glomeruli, a vector the size of the number of glomeruli was constructed with all zeros except for the most medial glomerulus. This vector was then multiplied by the kNN graph (weighting each cell by 0.1 and the influence of its nearest 10 neighbors by 0.9) and renormalized from 0 to 1; this procedure was repeated 1500 times until the values at each iteration remained stable. The resulting vector was rank-ordered, and these ranks were considered the ranks for each glomerulus along a single axis that spanned across the medial glomerular domain.

Sister glomeruli are matching pairs between the medial and lateral glomerular domains. Linear regression was performed to evaluate how well the ranks of each medial glomerulus could be predicted based on the positions of its corresponding lateral sister, to assess the conservation of the glomerular maps in each domain. To do so, support vector machine regression models (with a rbf kernel and C=1 regularization) were trained using 5-fold cross-validation on the z-scored lateral positions to predict the glomerular ranks.

Symmetric glomeruli are those that were identified in both the left and right OB. For these glomeruli, we could also evaluate to what extent nearest-neighbor relationships were preserved across the two OB. For each OB, pairwise distances were calculated for all pairs of glomeruli within the same domain, and these distances were compared across OB.

Comparisons of glomerular positions with OR genomic features

ORs were categorized as class I and class II based on their amino acid sequences. While class I ORs are located within a single genomic cluster on chromosome 7, class II ORs are located in genomic clusters that are scattered throughout the genome. ORs that were located on the same chromosome within 3 Mb of each other were defined as being within the same genomic cluster. Phylogenetic distances were calculated for pairs of OR, as previously described (Tsukahara et al 2023). In brief, phylogenetic trees were constructed from OR amino acid sequences, and the cophenetic distance of the resulting pairwise phylogenetic distance matrix was taken to be the phylogenetic distance between pairs of ORs. The distribution of phylogenetic distances was evaluated for pairs of class II ORs whose glomeruli were located at given spatial distances within the same OB domain. Additionally, for each OR genomic cluster, the mean phylogenetic and glomerular distance were evaluated for the set of OR pairs whose ORs were both from that genomic cluster. As an example, the OR cluster at Chr10:128.9–130.2 Mb contains ORs that are both phylogenetically and spatially similar to each other, and this cluster is enriched for the set of ORs that express *Cd36*.

Prediction of glomerular positions from OR transcriptomic features

Apart from genomic features, each OSN subtype is associated with a unique transcriptome, which can be summarized by the expression of a set of ~1,300 highly-variable genes (HVGs) whose expression varies across mature OSNs. These HVGs, and their mean expression for OSN subtypes expressing given ORs were evaluated from a recent single-cell RNA-sequencing (scRNA-seq) dataset, as previously described (Tsukahara et al. 2023). Linear regression was performed for geometrically-confirmed glomeruli to evaluate to what extent HVG expression for each OSN subtype could predict its respective glomerular positions in each OB domain. A scikit-learn regression pipeline was constructed in which, on training data, HVG expression for each OSN subtype was z-scored, the top 500 HVGs were selected, and PCA was performed to reduce the dimensionality of this data to 200 dimensions. Elastic net linear regression models (l1_ratio=0.05, alpha=1) were fit on these PCs, and the performance of this pipeline was then evaluated on held-out test ORs. Predicted positions for each glomerulus were evaluated using leave-one-out cross-validation separately for each domain (medial and lateral) for each axis (anterior-posterior and dorsal-ventral). Additionally, the median absolute error was evaluated for each axis in each domain across 100 restarts in which 20% of glomeruli were randomly held out.

OSNs expressing different ORs are thought to express different levels of axon guidance genes, which could influence the targeting of their axons to their respective glomerular positions. To more directly test this hypothesis, linear regression was also performed using only the expression of each axon guidance gene, as measured via scRNA-seq, as features. Axon guidance genes were defined as genes representing known axon guidance or cell adhesion molecules, and which included 183 genes that contained the following prefixes: *Slit, Robo, Epha, Ephb, Efn, Nrp, Sema, Plx, Kirrel, Pcdh, Cdh, Tenm*. Linear regression was performed as described above using a similar pipeline, except the gene feature selection step was omitted, only the top 50 PCs were kept, and the elastic net models were trained with an l1_ratio=0.01.

To group axon guidance and HVGs into sets of related genes, the predicted positions from the linear regression models were correlated with the observed positions for each domain and axis and the resulting correlation matrix was hierarchically clustered via scikit-learn's AgglomerativeClustering (with k=7 clusters). To summarize the average expression of genes associated with each cluster, the gene expression for each gene was z-scored across glomeruli and then averaged for each cluster. For example, the resulting cluster 2 was enriched for genes whose expression was the highest in OSN subtypes whose glomeruli projected to the anterior OB, whereas the expression of genes in cluster 6 was the highest for OSN subtypes enriched in the medial region of the OB. For visualization purposes, the

average gene expression for each OSN subtype was plotted on the OB maps at the locations of its associated glomeruli. A similar approach was also used to identify HVGs whose expressions across OSN subtypes was highly-correlated with glomerular positions.

Gene expression analysis of deep layer structure

Rotating axis differential expression analysis

Sections 38 to 147 were subset from the full dataset for deep layer analysis to avoid potential artifacts from non-OB regions like accessory olfactory bulb (AOB) and anterior olfactory nucleus (AON). Capture spots from Leiden Clusters 1, 8&9, and 6 were isolated from the full dataset and analyzed based on their morphological alignment to the deep granule cell layer, superficial granule cell layer, and mitral cell layer (respectively). For each cluster/layer, the 110-section dataset was collapsed along the z-axis into a 3D plane.

For each OB (right and left), axes were imposed onto the data at 10 prespecified rotation angles from 0˚ to 180˚ (i.e., 0˚, 18˚, 36˚... 162˚, 180˚). For each angle, differential expression analysis (DEA) was performed using the Wilcoxon Rank Sum Test for capture spots distributed on each sides of the axis. This analysis produced DEA with log2FC and adjusted p-value for each gene at each of the prespecified axis angles. This output was then filtered to only axes with adjusted p-value less than 0.05. Then, for each gene, the analysis was filtered to retain the top axis angle which generated the DEA result with the largest absolute log2FC value. Finally, the gene/axis pairs with the top 50 largest absolute log2FC values were retained for visualization.

REFERENCES

1. Formisano, E. *et al.* Mirror-symmetric tonotopic maps in human primary auditory cortex. *Neuron* **40**, 859–869 (2003).
2. Hasson, U., Harel, M., Levy, I. & Malach, R. Large-scale mirror-symmetry organization of human occipito-temporal object areas. *Neuron* **37**, 1027–1041 (2003).
3. Geschwind, N. & Levitsky, W. Human brain: left-right asymmetries in temporal speech region. *Science* **161**, 186–187 (1968).
4. Ocklenburg, S., Ströckens, F. & Güntürkün, O. Lateralisation of conspecific vocalisation in non-human vertebrates. *Laterality* **18**, 1–31 (2013).
5. Walker, S. F. Lateralization of functions in the vertebrate brain: a review. *Br. J. Psychol. Lond. Engl. 1953* **71**, 329–367 (1980).
6. Güntürkün, O. & Ocklenburg, S. Ontogenesis of Lateralization. *Neuron* **94**, 249–263 (2017).
7. Manns, M. & Ströckens, F. Functional and structural comparison of visual lateralization in birds - similar but still different. *Front. Psychol.* **5**, 206 (2014).
8. Bianco, I. H. & Wilson, S. W. The habenular nuclei: a conserved asymmetric relay station in the vertebrate brain. *Philos. Trans. R. Soc. Lond. B. Biol. Sci.* **364**, 1005–1020 (2009).
9. Halpern, M. E., Liang, J. O. & Gamse, J. T. Leaning to the left: laterality in the zebrafish forebrain. *Trends Neurosci.* **26**, 308–313 (2003).
10. Chess, A., Simon, I., Cedar, H. & Axel, R. Allelic inactivation regulates olfactory receptor gene expression. *Cell* **78**, 823–834 (1994).
11. Monahan, K. & Lomvardas, S. Monoallelic expression of olfactory receptors. *Annu. Rev. Cell Dev. Biol.* **31**, 721–740 (2015).
12. Buck, L. & Axel, R. A novel multigene family may encode odorant receptors: a molecular basis for odor recognition. *Cell* **65**, 175–187 (1991).
13. Mombaerts, P. *et al.* Visualizing an olfactory sensory map. *Cell* **87**, 675–686 (1996).
14. Ressler, K. J., Sullivan, S. L. & Buck, L. B. Information coding in the olfactory system: evidence for a stereotyped and highly organized epitope map in the olfactory bulb. *Cell* **79**, 1245–1255 (1994).
15. Serizawa, S. *et al.* Mutually exclusive expression of odorant receptor transgenes. *Nat. Neurosci.* **3**, 687–693 (2000).
16. Vassar, R. *et al.* Topographic organization of sensory projections to the olfactory bulb. *Cell* **79**, 981–991 (1994).
17. Wang, I.-H. *et al.* Spatial transcriptomic reconstruction of the mouse olfactory glomerular map suggests principles of odor processing. *Nat. Neurosci.* **25**, 484–492 (2022).
18. Zhu, K. W. *et al.* Decoding the olfactory map through targeted transcriptomics links murine olfactory receptors to glomeruli. *Nat. Commun.* **13**, 5137 (2022).
19. Dikeçligil, G. N. *et al.* Odor representations from the two nostrils are temporally segregated in human piriform cortex. *Curr. Biol. CB* **33**, 5275-5287.e5 (2023).
20. Grobman, M. *et al.* A Mirror-Symmetric Excitatory Link Coordinates Odor Maps across Olfactory Bulbs and Enables Odor Perceptual Unity. *Neuron* **99**, 800-813.e6 (2018).

21. Schoenfeld, T. A., Clancy, A. N., Forbes, W. B. & Macrides, F. The spatial organization of the peripheral olfactory system of the hamster. Part I: Receptor neuron projections to the main olfactory bulb. *Brain Res. Bull.* **34**, 183–210 (1994).

22. Schoenfeld, T. A. & Cleland, T. A. The anatomical logic of smell. *Trends Neurosci.* **28**, 620–627 (2005).

23. Haddad, R. *et al.* Olfactory cortical neurons read out a relative time code in the olfactory bulb. *Nat. Neurosci.* **16**, 949–957 (2013).

24. Nagai, Y., Sano, H. & Yokoi, M. Transgenic expression of Cre recombinase in mitral/tufted cells of the olfactory bulb. *genesis* **43**, 12–16 (2005).

25. Zeppilli, S. *et al.* Molecular characterization of projection neuron subtypes in the mouse olfactory bulb. *eLife* **10**, e65445 (2021).

26. Danciger, E., Mettling, C., Vidal, M., Morris, R. & Margolis, F. Olfactory marker protein gene: its structure and olfactory neuron-specific expression in transgenic mice. *Proc. Natl. Acad. Sci. U. S. A.* **86**, 8565–8569 (1989).

27. Wensley, C. H. *et al.* Olfactory marker protein mRNA is found in axons of olfactory receptor neurons. *J. Neurosci. Off. J. Soc. Neurosci.* **15**, 4827–4837 (1995).

28. Abdus-Saboor, I. *et al.* An Expression Refinement Process Ensures Singular Odorant Receptor Gene Choice. *Curr. Biol. CB* **26**, 1083–1090 (2016).

29. Ibarra-Soria, X., Levitin, M. O., Saraiva, L. R. & Logan, D. W. The olfactory transcriptomes of mice. *PLoS Genet.* **10**, e1004593 (2014).

30. Bozza, T., Feinstein, P., Zheng, C. & Mombaerts, P. Odorant receptor expression defines functional units in the mouse olfactory system. *J. Neurosci. Off. J. Soc. Neurosci.* **22**, 3033–3043 (2002).

31. Feinstein, P. & Mombaerts, P. A contextual model for axonal sorting into glomeruli in the mouse olfactory system. *Cell* **117**, 817–831 (2004).

32. Zamparo, I. *et al.* Axonal Odorant Receptors Mediate Axon Targeting. *Cell Rep.* **29**, 4334-4348.e7 (2019).

33. Ngai, J., Dowling, M. M., Buck, L., Axel, R. & Chess, A. The family of genes encoding odorant receptors in the channel catfish. *Cell* **72**, 657–666 (1993).

34. Zhang, X. & Firestein, S. The olfactory receptor gene superfamily of the mouse. *Nat. Neurosci.* **5**, 124–133 (2002).

35. Bozza, T. *et al.* Mapping of class I and class II odorant receptors to glomerular domains by two distinct types of olfactory sensory neurons in the mouse. *Neuron* **61**, 220–233 (2009).

36. Tsuboi, A., Miyazaki, T., Imai, T. & Sakano, H. Olfactory sensory neurons expressing class I odorant receptors converge their axons on an antero-dorsal domain of the olfactory bulb in the mouse. *Eur. J. Neurosci.* **23**, 1436–1444 (2006).

37. Xavier, A. M. *et al.* CD36 is expressed in a defined subpopulation of neurons in the olfactory epithelium. *Sci. Rep.* **6**, 25507 (2016).

38. Horgue, L. F. *et al.* Transcriptional adaptation of olfactory sensory neurons to GPCR identity and activity. *Nat. Commun.* **13**, 2929 (2022).

39. Tsukahara, T. *et al.* A transcriptional rheostat couples past activity to future sensory responses. *Cell* **184**, 6326-6343.e32 (2021).

40. Cloutier, J.-F. *et al.* Differential requirements for semaphorin 3F and Slit-1 in axonal targeting, fasciculation, and segregation of olfactory sensory neuron projections. *J. Neurosci. Off. J. Soc. Neurosci.* **24**, 9087–9096 (2004).

41. Nguyen-Ba-Charvet, K. T., Di Meglio, T., Fouquet, C. & Chédotal, A. Robos and slits control the pathfinding and targeting of mouse olfactory sensory axons. *J. Neurosci. Off. J. Soc. Neurosci.* **28**, 4244–4249 (2008).

42. Walz, A., Feinstein, P., Khan, M. & Mombaerts, P. Axonal wiring of guanylate cyclase-D-expressing olfactory neurons is dependent on neuropilin 2 and semaphorin 3F. *Dev. Camb. Engl.* **134**, 4063–4072 (2007).

43. Bashkirova, E. V. *et al.* Opposing, spatially-determined epigenetic forces impose restrictions on stochastic olfactory receptor choice. *eLife* **12**, RP87445 (2023).

44. Oka, Y. *et al.* O-MACS, a novel member of the medium-chain acyl-CoA synthetase family, specifically expressed in the olfactory epithelium in a zone-specific manner. *Eur. J. Biochem.* **270**, 1995–2004 (2003).

45. Serizawa, S. *et al.* A neuronal identity code for the odorant receptor-specific and activity-dependent axon sorting. *Cell* **127**, 1057–1069 (2006).

46. Belluscio, L., Lodovichi, C., Feinstein, P., Mombaerts, P. & Katz, L. C. Odorant receptors instruct functional circuitry in the mouse olfactory bulb. *Nature* **419**, 296–300 (2002).

47. Belluscio, L. & Katz, L. C. Symmetry, stereotypy, and topography of odorant representations in mouse olfactory bulbs. *J. Neurosci. Off. J. Soc. Neurosci.* **21**, 2113–2122 (2001).

48. Lodovichi, C., Belluscio, L. & Katz, L. C. Functional topography of connections linking mirror-symmetric maps in the mouse olfactory bulb. *Neuron* **38**, 265–276 (2003).

49. Parthasarathy, K. & Bhalla, U. S. Laterality and symmetry in rat olfactory behavior and in physiology of olfactory input. *J. Neurosci. Off. J. Soc. Neurosci.* **33**, 5750–5760 (2013).

50. Rajan, R., Clement, J. P. & Bhalla, U. S. Rats smell in stereo. *Science* **311**, 666–670 (2006).

51. Palmer, A. R. Symmetry Breaking and the Evolution of Development. *Science* **306**, 828–833 (2004).

52. Roussigne, M., Blader, P. & Wilson, S. W. Breaking symmetry: the zebrafish as a model for understanding left-right asymmetry in the developing brain. *Dev. Neurobiol.* **72**, 269–281 (2012).

53. Szenker-Ravi, E. *et al.* Discovery of a genetic module essential for assigning left-right asymmetry in humans and ancestral vertebrates. *Nat. Genet.* **54**, 62–72 (2022).

54. Chen, Y. *et al.* High-throughput sequencing of single neuron projections reveals spatial organization in the olfactory cortex. *Cell* **185**, 4117-4134.e28 (2022).

55. Igarashi, K. M. *et al.* Parallel mitral and tufted cell pathways route distinct odor information to different targets in the olfactory cortex. *J. Neurosci. Off. J. Soc. Neurosci.* **32**, 7970–7985 (2012).

56. Egger, V. & Urban, N. N. Dynamic connectivity in the mitral cell–granule cell microcircuit. *Semin. Cell Dev. Biol.* **17**, 424–432 (2006).

57. Geramita, M. A., Burton, S. D. & Urban, N. N. Distinct lateral inhibitory circuits drive parallel processing of sensory information in the mammalian olfactory bulb. *eLife* **5**, e16039 (2016).

58. Schoppa, N. E. & Urban, N. N. Dendritic processing within olfactory bulb circuits. *Trends Neurosci.* **26**, 501–506 (2003).

59. Francia, S. & Lodovichi, C. The role of the odorant receptors in the formation of the sensory map. *BMC Biol.* **19**, 174 (2021).

60. Mombaerts, P. Axonal wiring in the mouse olfactory system. *Annu. Rev. Cell Dev. Biol.* **22**, 713–737 (2006).

61. Sakano, H. Neural map formation in the mouse olfactory system. *Neuron* **67**, 530–542 (2010).

62. Wang, F., Nemes, A., Mendelsohn, M. & Axel, R. Odorant receptors govern the formation of a precise topographic map. *Cell* **93**, 47–60 (1998).

63. He, D. *et al.* Alevin-fry unlocks rapid, accurate and memory-frugal quantification of single-cell RNA-seq data. *Nat. Methods* **19**, 316–322 (2022).

64. Brann, D. H. *et al.* Non-neuronal expression of SARS-CoV-2 entry genes in the olfactory system suggests mechanisms underlying COVID-19-associated anosmia. *Sci. Adv.* **6**, eabc5801 (2020).

65. Schindelin, J. *et al.* Fiji: an open-source platform for biological-image analysis. *Nat. Methods* **9**, 676–682 (2012).

66. Arganda-Carreras, I. *et al.* Consistent and Elastic Registration of Histological Sections Using Vector-Spline Regularization. in *Computer Vision Approaches to Medical Image Analysis* (eds. Beichel, R. R. & Sonka, M.) vol. 4241 85–95 (Springer Berlin Heidelberg, Berlin, Heidelberg, 2006).

67. Boergens, K. M. *et al.* webKnossos: efficient online 3D data annotation for connectomics. *Nat. Methods* **14**, 691–694 (2017).